In vitro formation and extended culture of highly metabolically active and contractile tissues

Isabella A. Bagdasarian[1], Thamidul Islam Tonmoy[1], B. Hyle Park[1], Joshua T. Morgan[1*]

[1]Department of Bioengineering, University of California, Riverside, CA 92521

* Corresponding author: jmorgan@engr.ucr.edu (JTM)

Abstract

3D cell culture models have gained popularity in recent years as an alternative to animal and 2D cell culture models for pharmaceutical testing and disease modeling. Polydimethylsiloxane (PDMS) is a cost-effective and accessible molding material for 3D cultures; however, routine PDMS molding may not be appropriate for extended culture of contractile and metabolically active tissues. Failures can include loss of culture adhesion to the PDMS mold and limited culture surfaces for nutrient and waste diffusion. In this study, we evaluated PDMS molding materials and surface treatments for highly contractile and metabolically active 3D cell cultures. PDMS functionalized with polydopamine allowed for extended culture duration (14.8 ± 3.97 days) when compared to polyethylamine/glutaraldehyde functionalization (6.94 ± 2.74 days); Additionally, porous PDMS extended culture duration (16.7 ± 3.51 days) compared to smooth PDMS (6.33 ± 2.05 days) after treatment with TGF-β2 to increase culture contraction. Porous PDMS additionally allowed for large (13 mm tall × 8 mm diameter) constructs to be fed by diffusion through the mold, resulting in increased cell density (0.0210 ± 0.0049 mean nuclear fraction) compared to controls (0.0045 ± 0.0016 mean nuclear fraction). As a practical demonstration of the flexibility of porous PDMS, we engineered a vascular bioartificial muscle model (VBAM) and demonstrated extended culture of VBAMs anchored with porous PDMS posts. Using this model, we assessed the effect of feeding frequency on VBAM cellularity. Feeding 3×/week significantly increased nuclear fraction at multiple tissue depths relative to 2×/day. VBAM maturation was similarly improved in 3×/week feeding as measured by nuclear alignment (23.49° ± 3.644) and nuclear aspect ratio (2.274 ± 0.0643) relative to 2x/day (35.93° ± 2.942) and (1.371 ± 0.1127), respectively. The described techniques are designed to be simple and easy to implement with minimal training or expense, improving access to dense and/or metabolically active 3D cell culture models.

Introduction

Animal models have long been mainstays of biomedical research. While *in vivo* model systems by their nature include important systemic factors, they often fail to recapitulate the physiology of human tissues [1,2]. There is variability in how animals develop pathologies and respond to pharmaceuticals, compared to humans [3–5]. For example, the cholesterol lowering drug cerivastatin was withdrawn from the US market in 2001 after cases of fatal rhabdomyolysis were reported, despite minimal adverse effects being observed in preclinical animal studies [6–10]. Two-dimensional (2D) *in vitro* cell culture systems are linked to increased throughput, cost-effectiveness, and experimental simplicity [11–14]. Despite these clear advantages, 2D models are also associated with poor drug sensitivity [13–15], improper cellular organization and morphology [16], and altered gene and protein expression [14,17,18]. In response to these limitations and other needs, significant effort has been placed in the development of 3-dimensional (3D) cell culture models as an additional tool. These systems circumvent the systemic variables, timescale, and ethical challenges associated with animal models, while providing increased physiological relevance compared to conventional *in vitro* methods. [14,17].

3D tissue culture and organoid formation have become increasingly relevant tools to model complex tissues *in vitro* [19]. Despite progress, several engineering challenges remain. Many tissues have dense cell populations, which are difficult to mimic *in vitro*, due to the high contractile loads produced by cells, leading to collapse of a structured tissue [20]. Uncontrolled contraction of 3D collagen yields highly variable and unreproducible cultures [21]. Specifically, it is well documented that 3D culture collapse alters cell density and hydrogel porosity, due to the reduced volume of the culture [21,22]. Ultimately, this compromises the intended geometry and microarchitecture of the culture, and limits overall maturation of the tissue [21–23]. Uncontrolled

matrix contraction becomes especially problematic when fabricating naturally contractile cultures, including striated muscle (e.g. skeletal or cardiac muscle) and fibrosis models.

In vitro engineered tissues and 3D cell cultures are often formed within a mold, such as polydimethylsiloxane (PDMS). PDMS is a favorable molding material due to its accessibility, biocompatibility, low-cost, optical transparency, and tunable mechanical properties [24,25]. Yet, the innate hydrophobicity of PDMS does not promote long term adhesion of hydrophilic extracellular matrix proteins and cells, necessitating the need for separate functionalization steps. Immobilization of 3D cultures to a PDMS mold is frequently accomplished through chemical modification of the surface. One of the most common methods of chemical functionalization is polyethylenemine-glutaraldehyde (PEI/GA) crosslinking of collagen to a PDMS mold, although several other techniques exist for varying biomaterials [26]. Importantly, glutaraldehyde surface treatments are associated with potential adverse health risks [27–29] and negative environmental impacts [30,31]. Further, PEI/GA treatments are not always successful in immobilizing cell-laden collagen gels during extended culture with high cell densities [32].

Polydopamine (PDA), a bioinspired coating agent, is a potential alternative to PEI/GA. A wide variety of material surfaces (including PDMS) can be made adhesive to a broad range of biomolecules via simple dip-coating into an aqueous PDA solution [33]. Importantly, this coating technique does not require specialized equipment, making it accessible to a broad group of researchers. Dual functionalization of PDMS surfaces with PDA and ECM protein films such as collagen I or gelatin have previously been shown to improve adhesion and longevity of 2D cell culture studies [25,34–37]. However, it has not yet been demonstrated that PDMS coated with PDA improves the bulk anchoring of 3D cell culture matrix.

Surface roughness of PDMS varies with the fabrication and molding methods, but is generally in the range of 1-20 nm [38–41]. Limited PDMS surface roughness contributes to poor collagen adherence, resulting in hydrogel collapse under cell-generated loads. It has recently been demonstrated that increasing the surface roughness of the PDMS bulk improves collagen film adhesion in 2D [39]. Porous PDMS (P-PDMS) is known to have increased surface roughness and can be readily fabricated through the incorporation of sacrificial structures, such as water, salt, or sugar. Importantly, cells seeded in P-PDMS scaffolds have improved biomolecule and cell adhesion relative to normally fabricated smooth PDMS (S-PDMS) [41–44]. Yet, P-PDMS scaffolds as a molding material for bulk anchoring of 3D cell cultures in collagen have not been previously investigated. Improved anchoring may be especially beneficial for 3D cultures.

Indeed, strong anchoring of hydrogels to matrix attachment points is especially relevant for engineering contractile tissues, such as skeletal muscle. Tissue engineered skeletal muscle constructs, termed bioartificial muscle models (BAMs), are fabricated from undifferentiated muscle cells (myoblasts) suspended in an extracellular matrix and cast around anchor points within a simple cylindrical mold [45]. These anchors maintain passive tension within the differentiating tissue. In recent years, the matrix anchoring points have been fabricated from a variety of different materials, including: S-PDMS posts [46–48], 3D printed plastics [49] and hydrogels [50], mesh [51,52], velcro [53–55], and silk sutures [56,57]. Although many of these systems are low-cost and simple to fabricate, there have been reports of the engineered muscle rupturing off the anchors, especially when seeded at higher densities [52,58,59]. P-PDMS may mitigate incidences of tissue rupture due to its increased surface area, allowing for extended culture and maturation of the constructs.

In addition to collagen detachment, 3D cultures also exhibit increased metabolic demands. A well known limitation of 3D cultures and tissue is the diffusion limit; that is, cells do not receive adequate nutrient delivery or waste clearance beyond a few hundred microns of thickness in static culture conditions [60–64]. These challenges hinder the scalability and duration these tissues can be cultured *in vitro*. Efforts to support the metabolic activity of *in vitro* tissues often focus on the development of optimized culture media blends [65,66]; media supplements such as insulin, transferrin, selenium, glucocorticoids, vitamins, and pH buffers are known to improve cell growth and metabolism [65]. Further, optimization of feeding may improve cell and tissue health in 3D culture. Often, this is accomplished through the addition of direct tissue perfusion systems designed to increase mass transport within the culture. Perfusion systems have been incorporated in engineered bone [67–69], cartilage [70,71], cardiac [72], and skeletal muscle [73] and have been thoroughly reviewed [74–76]. Despite progress, perfusion systems are often optimized for specific research needs and are difficult for non-specialist research groups to utilize. P-PDMS can be fabricated to have interconnected pores [77–79]. With interconnected pores, there is the potential for P-PDMS to allow for media diffusion through the adhesion surface of the mold.

In this study, we validate the use of P-PDMS as a molding material to support contractile and metabolically active cultures in 3D collagen. Specifically, we compare PEI/GA and PDA chemistries for their ability to stably support contractile cells at high density. Further, we demonstrate that culture media can diffuse through the P-PDMS mold materials, improving health of metabolically active 3D cultures. As a further test case, we demonstrate P-PDMS as suitable anchor points for long term culture of vascularized BAMs (VBAMs); and demonstrate the effect of feeding frequency on skeletal muscle maturation over 5 weeks. Overall, we demonstrate PDA

126 treated P-PDMS molds as a simple and adaptable strategy in 3D cultures, especially where PEI/GA
127 treated S-PDMS molding is unsuitable due to contractile or metabolic concerns.
128

Materials and Methods

Collagen isolation

Collagen Type I was isolated from rat tail tendons as previously described [26,80,81]. Briefly, collagen fibers were retrieved from the fibers of rat tail (Pel-Freez Biologicals, Rogers, AR) tendons and soaked in 1x PBS. Afterwards, fibers were incubated in acetone and 70% isopropanol for 5 min each. Fibers were split evenly among conical tubes and swelled in 0.1% glacial acetic acid for 7 d on a rocker at 4°C. Dissolved collagen was centrifuged at ~20,000 x g for 1 h at 4°C to remove impurities. The collagen-containing supernatant was frozen at -80°C overnight and lyophilized to generate a collagen sponge. Prior to use, collagen sponges were dissolved in 0.1% glacial acetic acid to 8 mg/mL and stored at 4°C.

Cell culture

All cells were routinely cultured at 37°C and 5% CO_2. IMR90s (human lung myofibroblast; passage 17-19; ATCC, VA, USA), MDCKs (canine kidney epithelial; ATCC), HMEC1s (human microvascular endothelial; passage 8-10; ATCC), C2C12s (mouse myoblasts; passage 19; ATCC), and ASC52telos (human adipose derived stem cells; passage 7, ATCC), were maintained in their respective media blends (S1 Table) prior to 3D culture.

Fluorescent expressing C2C12s and HMEC1 cells were generated using lentiviral transduction. Transgenes were transduced into cells through 2nd generation lentiviral system. Briefly, 70% confluent HEK293TN (System Biosciences, Palo Alto, CA) cells were triple transfected (TransIT-Lenti, Mirus Bio, Madison, WI) with plasmids for viral packaging (psPAX2 was a gift from Didier Trono; Addgene plasmid #12260; http://n2t.net/addgene:12260; RRID:Addgene_12260), viral envelope (pMD2.G was a gift from Didier Trono; Addgene plasmid

#12259; http://n2t.net/addgene:12259; RRID:Addgene_12259). At 48 and 72 h post transfection, viral supernatant was collected, centrifuged to remove cellular debris, and filtered through a 0.45 μm cellulose acetate filter (Corning). Viral particles were stored at 4°C and used within 48 h by addition to culture media at a 1:2 ratio. Fluorescent expressing C2C12s were created by introducing copGFP (pCDH-EF1-copGFP-T2A-Puro was a gift from Kazuhiro Oka (Addgene plasmid # 72263; http://n2t.net/addgene:72263; RRID:Addgene_72263) and fluorescent HMEC1s were created by introducing mCherry (pCDH-CMV-mCherry-T2A-Puro was a gift from Kazuhiro Oka (Addgene plasmid # 72264; http://n2t.net/addgene:72264 ; RRID:Addgene_72264) plasmids. Positively expressing cells were selected using Puromycin at 1 μg/mL (C2C12 cells) or 0.1 μg/mL (HMEC1 cells) for 2 weeks.

S-PDMS mold fabrication & surface treatments

PDMS (Sylgard 184; Dow Corning, Midland MI) prepolymer was molded around a 3D printed mold (acrylonitrile butadiene styrene) creating wells 7 mm in diameter and 1.5 mm deep. S-PDMS was cured in the oven for 48 h at 55 °C and autoclaved prior to functionalization with (poly)ethylenimine/glutaraldehyde (PEI/GA) or polydopamine (PDA). Briefly, naïve S-PDMS molds were incubated in 2% PEI for 30 min, rinsed 3 times with autoclaved deionized water, dried, and immersed in 0.2% GA for 1 h, rinsed, and dried again [26,32]. Alternatively, naïve S-PDMS molds were incubated overnight in 2 mg/mL PDA solution made from dopamine hydrochloride (Sigma-Aldrich, St. Louis, MO) in 10 mM Tris Buffer (pH ~8.5; Apex Bioresearch Products, Boston, MA) as previously described [25]. S-PDMS molds were rinsed in autoclaved deionized water and dried prior to cell culture.

Figure 1. Fabrication of S-PDMS and P-PDMS molds. (A) PDMS pre-polymer is cast around a sugar cube template and thermally cured. Sugar granules are leached out in water and the molds are dried, revealing P-PDMS. (B) P-PDMS is molded around a 3D print to form wells 7 mm in diameter and 1.5 mm tall. (C) S-PDMS is molded around a 3D print to form VBAM outer chambers (20 mm x 1 mm x 1.5 mm). P-PDMS posts are punched to be 1/8" in diameter and adhered to glass inside the S-PDMS outer chambers.

P-PDMS mold fabrication

Two methods were used to form P-PDMS molds for 3D cell culture and are described in detail in Supplemental Methods (S1 File). Briefly, granulated sugar and sugar cubes were used as a sacrificial template to generate pores in molded PDMS (Fig 1). For collagen contractility studies granulated sugar was packed around a 3D printed mold (Fig 1B) and PDMS prepolymer was poured onto the sugar and around the mold and cured at 55°C. The P-PDMS was demolded from the 3D print and leached in water for 7 d at 40° C (Fig 1A). P-PDMS molds were adhered to 22 mm x 40 mm glass coverslips with a thin layer of PDMS prepolymer, cured in the oven, and autoclaved prior to functionalization as described above. For 3D culture metabolic studies, P-PDMS was fabricated using sugar cubes as a sacrificial template to ensure pores were interconnected [82–84]. After leaching in water, 3D culture molds were formed using a 1/4 in punch to create a well for collagen cultures, cut to be 1/2 in tall, then adhered to glass coverslips (22 mm x 40 mm) with PDMS prepolymer (Fig 1A). Prior to PDA functionalization, P-PDMS was rewet in an ethanol gradient. VBAM mold posts were also fabricated from P-PDMS sugar cubes. Posts for matrix attachment were made using a 1/8 in diameter punch and cut to be ~3 mm tall. Posts were functionalized in PDA, dried, and were adhered to glass as described above. S-PDMS

outer chambers were fabricated from PDMS prepolymer molded around a 3D print design (acrylonitrile butadiene styrene). Each outer chamber has dimensions of 20 mm x 1 mm x 2.5 mm (LxWxH) (Fig 1C). After curing, S-PDMS was demolded and individual chambers were trimmed, placed around the posts, and autoclaved.

Assessment of PDMS surface treatments

S-PDMS molds were prepared and treated with either PEI/GA, PDA, or left naïve (control) as described. IMR90s were suspended in 3 mg/mL rat tail collagen type I at 2 x 10^6 cells/mL and gelled at 37°C for 30 min and then submerged in IMR90 medium (S1 Table). Cultures were monitored daily for loss of adhesion from the S-PDMS mold. Cultures were considered de-adhered when more than 270° of the perimeter had detached from the S-PDMS wall. Survival past this point was quantified relative to the number of days it took the naïve cultures to detach (Fig 2).

Figure 2. Loss of S-PDMS/collagen adhesion. (Top) IMR90s are seeded in a collagen matrix in a naïve S-PDMS mold. (Bottom) By day 6 of culture the collagen has completely unadhered from S-PDMS wall.

Assessment of P-PDMS/collagen adhesion

S-PDMS and P-PDMS molds were prepared, treated with PDA, and seeded with IMR90s at 2 x 10^6 cells/mL as described above. After gelation samples were submerged in IMR90 medium with/without 2 ng/mL TGF-β2 (100-35B; PeproTech, Cranbury, NJ). Cultures were monitored for loss of collagen adhesion and contraction of the gel for 21 d and survival was quantified as described above.

Assessment of P-PDMS nutrient diffusion

For metabolic studies, 13 mm tall × 8 mm diameter S-PDMS and P-PDMS molds were fabricated and seeded with MDCK cells at 2 x 10^6 cells/mL. In the case of the P-PDMS molds, collagen that leaked through the porous mold was cut away after gelation. The molds and collagen were placed in 12 well plates and media was added to be level with the mold surface, but not covering the culture (the top of the culture was at the air-liquid interface). Samples were fed at days 1,2, and 4 of culture. Media was isolated for downstream glucose assays at days 1 and 5. After 5 days of culture, samples were fixed for immunofluorescence.

VBAM model fabrication

To facilitate live imaging throughout culture, VBAMs were fabricated from C2C12s expressing copGFP and HMEC1 cells expressing mCherry. C2C12s, HMEC1s, and ASC52telos were trypsinized and suspended in a 2 mg/mL type I rat tail collagen matrix (3440-100-01; R&D Biosystems, Minneapolis, MN) at 10 x 10^6 cells/mL, 2 x 10^6 cells/mL, and 0.5 x 10^6 cells/mL, respectively. Cell laden collagen was seeded in S-PDMS chambers 20 mm x 1 mm x 2.5 mm around P-PDMS posts of 1/8 in diameter (Fig 1C). After a 60 minute gelation, constructs were submerged in VBAM growth media (S1 Table) supplemented with 1 ng/mL VEGF. VBAM growth media was exchanged every other day until day 5 of culture to allow for myoblast proliferation. At this time media was replaced with VBAM differentiation media (S1 Table). Microvessel self-assembly was promoted through VEGF supplementation for another 2 weeks before being replace with 0.1 ng/mL PDGF-BB for the remainder of the culture period [85,86]. These conditions were shown to result in robust microvessel networks in prior experiments without muscle cells (S1 Fig). After 3-4 days in differentiation media, S-PDMS chambers were removed to expose a larger surface area of the tissue to culture media. VBAMs were differentiated for 5 weeks prior to tissue fixation.

To test the effects of sample feeding frequency during differentiation we implemented the following media exchange regimes: 3x a week on Monday, Wednesday, and Friday (MWF), daily, or every 12 h (B.I.D). Feedings performed every 12 hrs were controlled via an automated syringe pump system described in detail in Supplemental Methods (S1 File).

3D culture fixation and staining

3D IMR90 cultures were fixed in 4% paraformaldehyde in PBS with 0.5% Triton X-100 *in situ* for 2 h at room temperature followed by an overnight permeabilization in 0.5% Triton X-100 in PBS at 4°C. Following fixation, samples were demolded and placed in 1.7 mL tubes and stained against F-actin and nuclei using Phalloidin and DRAQ7 in blocking buffer (S2 Table) on a rocker for 48 h at 4°C. 3D MDCK cultures were fixed 4% paraformaldehyde in PBS with 0.5% Triton X-100 *in situ* for 2 hr at room temperature followed by an overnight fixation and permeabilization in fresh 4% paraformaldehyde and 0.5% Triton X-100 in PBS at 4°C. After fixation, samples were demolded and transferred to a 48 well plate to maintain spatial orientation during staining. Nuclei were labeled with DRAQ7 as described above.

To ensure sufficient penetration of antibodies into VBAM models, we adopted a modified version of Dent's fixation [87,88]. Briefly, VBAMs were triple rinsed in PBS containing calcium and magnesium (21-030-CM; Corning). Samples were fixed *in situ* in [4:1] methanol and DMSO (BP231-1; Fisher BioReagents; Waltham, MA) at 4°C overnight. The following day VBAMs were demolded and transferred to a 24 well plate and dehydrated with 3x methanol incubations for 20 min at 4°C. After, samples were incubated in Dent's bleach solution consisting of [4:1:1] methanol:DMSO:30% hydrogen peroxide for 2 h at room temperature. Samples were rehydrated in a descending methanol gradient in PBS: 100%, 75%, 50%, 25% methanol and 100% 1× PBS for 10 min at room temperature, before incubating in blocking buffer for 2 h. VBAMs were stained

against markers of terminal muscle differentiation and for mCherry labeled HMEC1 cells (S2 Table) for 72 h on a rocker at 4°C followed by secondary antibody staining for 48 h on a rocker at 4°C (S2 Table).

Image acquisition, tissue clearing, and volumetric quantification

All samples were imaged on a Leica TCS SPE-II laser scanning confocal microscope (Leica, Buffalo Grove, IL). For 3D culture experiments with IMR90s, MDCKs, and VBAMs, a total volume of 0.5 mm^3, 3 - 7.5 mm^3, and 0.25 - 1.20 mm^3 were acquired, respectively. Samples were imaged in S-PDMS chambers attached to glass with PBS and acquisition settings were held constant within experimental groups. VBAM and MDCK experiments were imaged before and after clearing. Tissue clearing was performed similar to previously published protocols [89]. Briefly, samples were dehydrated in excess methanol on a rocker at 4°C 3× for 20 min. Samples were then transferred to glass petri dishes and cleared in methyl salicylate for 7× 10 min incubations at room temperature. Samples were imaged in methyl salicylate in S-PDMS chambers sealed to coverslip glass with silicone grease. Confocal tilescans were acquired of the culture base and stitched into a single volume for MDCK experiments. VBAMs were imaged end to end via sequential tilescans.

Prior to analysis all tilescan volumes were aligned and stitched together using a custom MATLAB implementation of the Phase Correlation Method previously described [90]. Nuclear volume fraction was quantified using custom algorithms. Detailed filtering and segmentation steps are described in Supplemental Methods (S1 File).

To quantify annular nuclear volume fraction in VBAMs, we first stitched and filtered tilescans as described in the Supplemental Methods (S1 File). Muscle bulk was segmented using the myosin or titin channel via hysteresis thresholding. Debris and artifacts were removed from

288 the binary muscle bulk volume with morphological opening and closing using a disk structuring
289 element of radius 1.79 μm and 5.38 μm, respectively. Similarly, the nuclei channel was segmented
290 via hysteresis thresholding and artifacts were removed. A Euclidean distance transform was
291 performed on the muscle bulk starting at the outer edge of the nuclear layer and used to determine
292 voxel location from the tissue surface. Annular rings moving from the tissue surface inwards were
293 spaced at 14.3 μm. Nuclear volume fraction was defined within each annulus. Annular nuclear
294 fraction was quantified for 5 annular rings, with a max depth of 75 μm (Fig 3).
295
296 **Figure 3. Annular nuclear volume fraction demonstration.** VBAM nuclei (transverse) and
297 muscle volumes are segmented. A distance transform is performed on the segmented muscle
298 volume to define how far each pixel in the tissue is from the tissue surface. Annular rings are
299 defined using the distance transform volume and integrated nuclear intensity is quantified within
300 them.
301 To quantify nuclear angle and aspect ratio we stitched and filtered the VBAM tilescans and
302 segmented the muscle bulk as described above, with an additional watershedding step to separate
303 individual nuclei. Nuclear eigenvectors and principal axis length were output. To account for tilt
304 in the acquired tilescans we solved for local muscle eigenvectors along the skeletonized muscle
305 volume. To accomplish this, we defined seed points at opposite edges of the muscle volume and
306 used an adaption of fast marching skeletonization previously described [32,91,92]. Local 3D
307 orientation along the skeletonization and nuclear angle was quantified as the orientation of the
308 major axis of a best fit ellipsoid. Nuclear aspect ratio was quantified by solving for the ratio of
309 nuclei major principal axis length to minor principal axis length, where a perfectly spherical nuclei

would have an aspect ratio equal to 1. Example code used to quantify VBAM annular nuclear volume fraction, nuclear angle, and aspect ratio is provided (S1 File).

Polarization-sensitive optical coherence tomography

To further assess myofiber alignment fixed and uncleared VBAM samples (two MWF and two B.I.D) were scanned with a custom-built spectral domain PS-OCT system, a detailed description of which is described in a previous report [93]. Detailed methods are provided in Supplemental Methods (S1 File). Briefly, post-processing was performed in MATLAB. The structural intensity images were generated with standard Fourier domain processing method [94–98] which shows the intensity of light backscattered from the samples. Muscle tissue also exhibits form birefringence [99], an optical property arising from the structural anisotropy of long, parallel fibrils embedded in a medium of different refractive index. PS-OCT can measure this phase retardation and optic axis [100–103] which are measures of the degree of organization and orientation of the fibrous structure, respectively. We used the spectral binning algorithm [104] to measure the local phase retardation ρ and optic axis θ, which were later combined for generating vectorial birefringence images [105].

For quantitative comparison, we used the phase retardation of the samples. In each cross-section, the tissue region was first identified using an intensity-based threshold of the background (60 dB). The average phase retardation inside these tissue regions were measured and plotted as a function of length of the samples in Fig S2A. The mean phase retardation over the length of the samples were then used for quantitatively comparing the two experimental groups.

Glucose assay

A colorimetric glucose assay (10009582; Cayman Chemical, Ann Arbor, MI) was performed to assess metabolic activity in 3D P-PDMS cultures. A detailed description of the glucose assay procedure can be found in Supplemental Methods (S1 File). Isolated media samples and control MDCK media were diluted in assay buffer and quantified on a plate reader (SpectraMax M2, Molecular Devices, San Jose, CA) at 513 nm relative to provided glucose standards.

Data analysis & statistics

For 3D IMR90 experiments, data was reported as mean days without collagen detachment ± SEM. PEI/GA and PDA surface treatments (n = 4) were tested for statistically significant differences using a paired sample t-test. Comparisons of S-PDMS and P-PDMS cultures (n = 3) were tested for statistically significant differences using a 2-way analysis of variance (ANOVA) followed by Tukey's honestly significant difference (HSD) *post hoc* test for effects of +/- TGF-β2 and S-PDMS vs P-PDMS cultures. Similarly, glucose assay (n = 3) results are reported as mean normalized absorbances and were tested using ANOVA followed by Tukey's HSD post hoc test. Nuclear fraction quantification is reported as mean ± SEM and assessed using a two-sample t-test For VBAMs each sample fabricated was treated as a biological replicate (n = 6). Phase retardation is reported as mean ± SEM (n = 2) and assessed using a two-sample t-test. Annular nuclear fraction, nuclear angle, and nuclear aspect ratio are reported as mean ± SEM and data was compared with a paired t-test (n = 6).

Results

Polydopamine surface treatment extends S-PDMS/collagen adhesion

S-PDMS surfaces were functionalized with PEI/GA or PDA and seeded with IMR90s suspended in a collagen gel, as described above. All samples were fed regularly and were monitored until loss of collagen adhesion. PEI/GA and PDA culture detachment was quantified relative to the detachment of naïve controls (e.g. days past naïve detachment). PEI/GA samples survived on 6.94 ± 2.74 days past naïve, while PDA cultures survived 14.8 ± 3.97 days (Fig 4A). To visualize the cell population in PDA samples, we fixed at day 4 and day 12 and stained for f-actin and nuclei. Confocal imaging of these samples revealed high cellularity with spread morphology and stress fibers, consistent with a dense, highly contractile culture (Fig 4B).

Fig 4. Effect of surface treatment and surface area on collagen adhesion. (A) Quantification of S-PDMS/collagen adhesion relative to the naïve control for each replicate reveals that samples in PDA molds maintained adherence longer than PEI-GA molds ($n = 4$, $p < 0.05$; paired sample t-test). Mean is indicated by black bars and triangle markers are data points. (B) PDA cultures were fixed at day 4 and day 12 and imaged for f-actin and nuclei. Representative intensity-based maximum projections qualitatively confirm cultures had high cell density at both time points **.** (C) IMR90s suspended in collagen gels molded by PDA treated S-PDMS or P-PDMS were fixed and stained for f-actin and nuclei at day 11. Representative intensity-based maximum projections demonstrate consistent cellularity regardless of molding method or TGF-β2 supplementation. (D) Culture survival was defined as the number of days samples lasted prior to loss of PDMS/collagen adhesion. Samples molded by P-PDMS exhibited increased survival, even when cultured in the

presence of TGF-β2. (n = 3, p <0.05; 2-way ANOVA and Tukey's HSD post hoc test). Mean is indicated by black bars and triangle markers are data points.

Porous PDMS extends PDMS/collagen adhesion during contractile culture

S-PDMS and P-PDMS molds were fabricated and treated with PDA prior to seeding with IMR90s in collagen. To increase culture contraction, samples were cultured without/with ((-)/(+)) 2 ng/mL TGF-β2 after day 1 of culture. Samples were fixed and stained against f-actin and nuclei at day 11 of culture to compare cellularity. Samples cultured with TGF-β2 ((+) TGF-β2) demonstrated a qualitative increase in stress fiber formation in both S-PDMS and P-PDMS molds (Figs 4C & 4D). There were no qualitative differences in cell density between S-PDMS and P-PDMS samples (-)/(+) TGF-β2. S-PDMS cultures (-) TGF-β had a mean time to detachment of 10.3 ± 4.22 days, the presence of TGF-β2 reduced that to 6.33 ± 2.05 days. P-PDMS cultures (-) TGF-β2 showed no indications of contraction or loss of adhesion with the mold; at day 21, all remaining cultures were ended. With TGF-β2, P-PDMS samples still demonstrated a significant increase in time before detachment when compared to S-PDMS (+) TGF-β2, 16.7 ± 3.51 days.

Cultures in porous PDMS molds can be maintained through side wall diffusion

To assess media diffusion in P-PDMS molds, 13 mm tall by 8 mm diameter PDMS molds were used. Both S-PDMS and P-PDMS wells were filled with cell-laden collagen; the P-PDMS molds had interconnected pores[82–84]. Media was added to the top level of the molds but did not cover the top surface, only diffusion through the mold was possible. On day 5, samples were fixed,

stained against nuclei, and cleared as described above. Confocal tilescans were acquired of the culture base and stitched into a single volume.

When compared to S-PDMS samples, P-PDMS samples had higher cell densities and well-formed spheroids, indicating robust cell growth (Fig 5A). To quantify this, nuclear volume fraction was quantified in both S-PDMS and P-PDMS samples (Figs 5B & S3); S-PDMS cultures had a mean nuclear fraction of 0.0045 ± 0.0016, while P-PDMS cultures had a mean value of 0.0210 ± 0.0049 ($p = 0.01$). To assess media depletion, culture media was isolated at day 1 and day 5 of culture to assay glucose levels (fresh media was added at day 0, day 1, day 2, and day 4). Glucose levels in S-PDMS cultures at days 1 and 5 was 64% and 45% of complete DMEM media at 4.5 g/L, while P-PDMS samples were 16% and 25% of complete media, respectively; these results indicate increased glycolysis of the P-PDMS cultures compared to S-PDMS, consistent with increased cell numbers and metabolism (Fig 5C).

Figure 5. Side wall diffusion through S-PDMS and P-PDMS molds. (A) MDCKs suspended in collagen gels molded by PDA treated S-PDMS or P-PDMS were fed through the side walls. After 7 days of culture, samples were fixed, stained for nuclei, and imaged from one end of the culture to the opposite end. Shown are intensity-based maximum projections of stitched tilescans (scalebar = 500 μM) and insets depict zoomed in regions. P-PDMS samples formed distinct spheroids, while S-PDMS sample nuclei remained sparse and scattered. (B) P-PDMS samples had increased nuclear volume fractions relative to S-PDMS ($n = 4$, $p < 0.01$; paired sample t-test).(C) Spent culture media was isolated from S-PDMS and P-PDMS samples at days 1 and 5. P-PDMS cultures consumed significantly more glucose than S-PDMS cultures ($n = 3$, $p < 0.05$, N-way ANOVA and Tukey's HSD post hoc test). Mean is indicated by black bars and triangle markers are data points.

Porous PDMS anchors VBAM cultures

As an additional demonstration of P-PDMS functionality, we fabricated P-PDMS posts to serve as matrix attachment sites for VBAMs (Fig 1C). Briefly, copGFP C2C12s, mCherry HMEC1s, and ASC52telos were suspended in a collagen matrix and seeded around P-PDMS posts inside a S-PDMS chamber at 12.5 million cells/mL total (Fig 1C). Despite its importance to tissue maturation, extended culture of dense skeletal muscle constructs remains a challenge due to the contractile nature of the tissue, causing it to rupture and detach from anchor points [52,58,59]. In this study, 24 VBAMs were cultured for 40 days without detachment, prior to downstream processing (Fig 6A). For a subset (n = 12) of this population, we observed maturation of the tissues via confocal live imaging of the endogenous fluorophores at days 2 and 21 of differentiation (Fig 6A). Early into the differentiation period, muscle cells can be seen stretching out to form myofibers, although void space and rounded cells remain. By day 21 no rounded cells remain, and myofibers are elongated and more compact. We also observed the formation of microvessel-like structures in fixed VBAMs; these structures were predominated localized to the VBAM surface (Figs 6B & 6C).

Fig 6. P-PDMS posts support VBAM culture. (A) Shown are intensity-based maximum projections of stitched tilescans encompassing ~25% of VBAM culture at days 2, 21, and 40 demonstrating stability throughout extended culture. (B) Intensity-based maximum projection of fixed VBAM shows vascular endothelial structures (mCherry) aligning parallel to myofibers (Myosin) (scalebar = 100 μM). (C) Segmented muscle and endothelial channels were used to

generate a 3D volume rendering. This 3D model demonstrates the predominant localization of vascular structures on the surface of the VBAM (0.2 mm x 0.4 mm x 0.5mm).

Increased feedings do not improve tissue maturation

We additionally tested the impact of feeding frequency on VBAM morphology and maturation. Maturation was evaluated via immunostaining against terminal differentiation markers, myosin (Figs 7A & 7B) or titin (Figs 7C & 7D). In cultures that were fed MWF we observed elongated myofibers with global alignment between the attachment posts (Figs 7A & 7C). Additionally, striations are present, consistent with sarcomere formation and functional maturity [106–108] (Figs 7A & 7C, insets). In contrast, B.I.D cultures have myoblasts appeared that have a more rounded shape with little alignment (Figs 7B & 7D, insets) and no visible striations; this is characteristic of undifferentiated myoblast cells (Figs 7B & 7D, insets).

To gain insight into VBAM nuclear alignment, we imaged cleared samples and quantified nuclear angle and nuclear aspect ratio. MWF VBAMs have a mean nuclear angle of 23.49° ± 3.64° and B.I.D VBAMs have a mean nuclear angle of 35.93° ± 2.94° (Fig 8E). MWF VBAMs have a mean nuclear aspect ratio of 2.27 ± 0.06 and B.I.D VBAMs have a mean value of 1.37 ± 0.11, further indicating MWF VBAMs have improved differentiation (Fig 7F).

Fig 7. Effects of feeding frequency on VBAM maturation. (A & C) After 5 weeks of culture VBAMs were fixed and stained against myosin (B & D) and titin. Intensity-based maximum projections of MWF VBAMs demonstrate highly aligned myofibers and the presence of striations (insets, white arrowhead). B.I.D VBAMs remained myoblast-like and mononucleated without striations (scalebar = 50 μm). (E) Nuclei in MWF VBAMs have increased alignment relative to

B.I.D nuclei (n=6, $p = 0.064$; paired sample t-test). (F) Nuclei in MWF VBAMs have an increased aspect ratio relative to B.I.D nuclei ($n = 6$, $p < 0.01$; paired sample t-test). Mean is indicated by black bars and triangle markers are data points.

To qualitatively and quantitatively analyze tissue scale fiber alignment, we analyzed PS-OCT data acquired from the uncleared samples. Figs 8A-H shows representative cross-sectional intensity, phase retardation, orientation, and vectorial birefringence images of MWF and B.I.D samples. The intensity images (Figs 8A & 8E) show the overall structure of the sample. From the phase retardation images (Figs 8B & 8F), we observe that the MWF samples have higher phase retardation (4.28 ± 0.47 rad/mm) than the B.I.D samples (1.78 ± 0.12 rad/mm) which demonstrate a statistically significant difference ($p = 0.04$) between the two experimental groups (Fig 8K). The difference in phase retardation agrees with the difference in morphology of the VBAMs observed in the immunostained images (Figs 7A-D). The structural anisotropy arising from the elongated myofibers causes higher phase retardation in the MWF samples. The phase retardation of the MWF samples is higher (>2.8 rad/mm) throughout the length of the samples compared to the B.I.D samples. One interesting characteristic of the MWF samples, is that the phase retardation in the middle of the samples is on average 20% higher compared to the two ends. This suggests that the muscle fibers are more organized and uniformly oriented in the middle as evident from the *en face* phase retardation images (S2B & S2C Figs).

The orientation images (Figs 8C & 8G) also exhibit more uniform fiber orientation in the MWF sample ($12.02° \pm 14.44°$) compared to the B.I.D sample ($21.69° \pm 35.37°$). This is also in line with the immunostained images (Figs 7A-D) where we observe well aligned elongated myofibers with striations in the MWF samples compared to rounded myoblasts with little

alignment and no striations in the B.I.D samples. The vectorial birefringence images (Figs 8D & 8H) combine the phase retardation and the optic axis images using HSV colormap. The cross-sectional vectorial birefringence images were compiled in Amira to generate the 3D vectorial birefringence images (Figs 8I-J). The uniformity in color throughout the volume of the MWF sample demonstrates the presence of more highly organized and uniformly orientated muscle fibers than the B.I.D sample.

Figure 8. PS-OCT analysis of the effects of feeding frequency on VBAM maturation. (A-D) shows representative cross-sectional intensity (in dB), phase retardation (in rad/mm), orientation (in degree) and vectorial birefringence images, respectively, from MWF sample (scalebar = 100 μm) (E-G) shows the similar cross-sections from B.I.D sample. The MWF samples exhibit higher phase retardation and more uniform orientation compared to the B.I.D samples (scalebar = 100 μm) . (I-J) shows representative 3D vectorial birefringence images of 4 mm long segment of MWF and B.I.D samples, respectively (scalebar = 500 μm). The MWF sample has highly organized and uniformly orientated muscle fibers throughout the volume compared to the B.I.D sample. (K) Quantification of the mean phase retardation of the MWF and B.I.D samples statistically improved differentiation ($p = 0.04$) in the MWF samples.

Increased feedings do not improve tissue viability

VBAM cellularity was evaluated using DRAQ7 to label cell nuclei in cleared samples. Volumes were acquired with a confocal microscope and transverse projections of nuclei signal were reconstructed in MATLAB (Fig 9A). In MWF tissues cell nuclei are detected throughout the bulk, but there is increased signal at the tissue surface. This indicates that myofibers are

preferentially located at the tissue exterior, consistent with cell organization noted in literature [54,109]. We observed 2 morphologies of nuclear organization in the B.I.D tissues. The first of which is that the constructs remained cellular (Fig 9A, B.I.D Morph. #1), but undifferentiated (Figs 7B & 8D). More commonly, there was a considerable decrease in nuclei signal (Fig 9A, B.I.D Morph. #2). To better assess the spatial distribution of cells, nuclei signal was segmented, and 3D volume renderings were generated (Figs 9B & S4), further confirming that MWF samples had improved cell organization. We additionally tried an intermediate feeding schedule with daily media changes, no improvement in cellularity over MWF was observed (S5 Fig).

To quantify volumetric cellularity, we measured the annular fraction of positively labeled nuclei voxels near the tissue surface (0-15 μm) and deeper into the tissue (15-30 μm, 30-45 μm, 45-60 μm, and 60-75 μm) (Fig 9C). In MWF samples, positive annular nuclear fraction at the tissue surface was significantly higher, with a value of 0.30 ± 0.04, relative to B.I.D, with a mean value of 0.03 ± 0.02. This trend continued at 10-20 μm and 20-30 μm deep into the samples, further supporting the observation that more frequent media changes led to decreased tissue cellularity.

Figure 9. Effects of feeding frequency on VBAM cellularity. (A) Representative transverse projections of VBAM nuclei demonstrate nuclei density and organization throughout the VBAM bulk. MWF VBAMs appear to have increased nuclei density relative to B.I.D morphology #1 and B.I.D morphology #2. (B) 3D volume renderings were generated to visualize the spatial organization of VBAM nuclei, further confirming that MWF VBAMs have increased nuclei density (1 mm x 0.5mm x 0.6 mm). (C) Annular nuclear fraction was quantified in increments of ~15 μm radiating inward from the VBAM surface. MWF VBAMs have a significantly higher annular nuclear fraction at 0-15 μm ($p < 0.01$), 15- 30 μm ($p < 0.01$), and 30-

45 μm ($p < 0.05$) than B.I.D VBAMs. Mean is indicated by bold blue and magenta lines with +/- SEM shown. Transparent lines show the mean annular nuclear fraction for individual biological replicates (n = 6, paired sample t-test).

Discussion

Improving 3D cell culture models provides researchers with an important tool for when animal models and traditional 2D culture models are inappropriate. For example, animal models provide important systemic context for disease progression and pharmaceutical response, yet high-throughput and detailed molecular studies can be challenging [2,110]. Similarly, 2D cell culture models offer increased simplicity and throughput, but lack critical systemic factors and native tissue characteristics (Soares *et al.*, 2012; Ravi *et al.*, 2015; Costa *et al.*, 2016; Jensen and Teng, 2020). Current progress in 3D cell culture models allow for the balancing of increased complexity and physiological relevance with increased control of *in vitro* systems. However, further development of these methods is required to expand applicability to more tissue types and increase researcher access. Key challenges addressed in this study include uncontrolled contraction of the extracellular matrix and mass transfer limitations. Here we introduce a novel culture system for 3D models, capable of supporting highly contractile myofibroblast cells using PDA coated P-PDMS and additionally demonstrate the use of P-PDMS molds to increase cell health in thick cultures. We further apply these techniques to skeletal muscle tissue engineering and demonstrate that PDA coated P-PDMS is a suitable matrix anchor for dense VBAM models. Finally, we evaluate the effect of tissue feeding frequency on overall VBAM health and organization.

Unconstrained cell-mediated gel contraction is a significant challenge with respect to 3D cell culture and tissue engineering [20]. Collapse of the extracellular matrix typically occurs in an uncontrolled manner, leading to highly variable outputs for the experiment [21]. In the context of skeletal muscle tissue engineering this problem is particularly detrimental, as it can result in tissue rupture, rendering the construct unusable. While researchers can address this problem by varying the culture length, ECM density, and seeding density, these may reduce maturation, physiological relevance, or otherwise limit the possible experimental conditions [32]. To address this, 3D culture molds are frequently surface modified to improve ECM adhesion to the mold interface. For instance, PEI/GA surface treatment is often used to improve adhesion of collagen biomaterials to S-PDMS molds [26], but this linkage still fails when seeding density or matrix stiffness is not optimal [32]. The bioinspired coating PDA has previously been used to anchor thin biomaterial films to S-PDMS but has not previously been shown to anchor 3D collagen-based cell cultures (Chuah *et al.*, 2015; Fu *et al.*, 2016; Jeong *et al.*, 2016; Lee *et al.*, 2018; Harati *et al.*, 2022). Here we demonstrate the novel application of using S-PDMS-PDA to anchor 3D collagen bulks under cell-mediated contractile loading. We evaluated the efficacy of S-PDMS-PEI/GA surface treatments in comparison to S-PDMS-PDA surface treatments and found that PDA coating significantly attenuated cell-mediated gel detachment (Figs 4A & 4B). S-PDMS-PDA is an improved collagen molding method when culturing dense 3D tissue constructs.

We further hypothesized that increased surface area of the PDMS molding material would improve collagen adhesion [111,112]. Prior work has shown P-PDMS can be used as a scaffold for 2D cell culture and cell migration studies [113–116]. However, P-PDMS has not previously been shown to be used as a molding material to anchor 3D collagen bulk matrices. To demonstrate this in the context of 3D collagen molding, we fabricated P-PDMS and examined PDA coated S-

PDMS and P-PDMS culture molds and maintained IMR90 cultures for up to 21 days before terminating the experiment. P-PDMS molding markedly improved collagen attachment (Figs 4C & 4D). P-PDMS as a mold offers improved collagen attachment for longer duration highly contractile cultures.

We were further interested in the impact of P-PDMS on mass transfer in 3D collagen cell culture models. Mass transfer limitations remains a fundamental problem for tissue engineering. Poor diffusion of nutrients and waste products result in cell death deep in cultures and chemotaxis to the more nutrient rich regions of the tissue [60–64]. While bioreactors and tissue perfusion can help resolve this issue, these techniques are not always readily available to non-specialist labs and may not be appropriate for all experiments. Here we describe the novel use of a P-PDMS mold capable of supporting cultures solely via diffusion through the side wall of the mold, keeping the top of the culture at the air-liquid interface (Figs 5 & S3). While still diffusion limited, the easy fabrication of permeable culture molds allows for increasing the scale of a culture or the incorporation of air-liquid interfaces. Potential applications include epithelial and stromal co-cultures where the epithelium is brought to the air-liquid interface, but the culture is too thick to be fed purely through a permeable support (e.g., a cell culture insert).

P-PDMS-PDA is also adaptable for 3D skeletal muscle cultures, a challenging *in vitro* model due to the high contractility. As a proof of concept, we showed that P-PDMS-PDA can be used at matrix attachment points for VBAMs, with no evidence of tissue rupture or detachment after 5 weeks of culture (Fig 6). In an effort to improve VBAM maturation and cellularity in the absence of tissue perfusion, we evaluated the effect of media change frequency. We initially hypothesized that more frequent feeding of the VBAM tissues would enhance myotube differentiation (Fig 7) and cellular organization (Figs 9 & S4), yet we observed an adverse effect. This lack of maturation

with increased feeding volume, while surprising, has been observed before [117]. While the mechanism is unknown, one possibility is the loss of paracrine signals vital to muscle differentiation that accumulate in the culture media; regular removal of those factors too quickly may impair overall VBAM health. Alternatively, the more frequent feeding may mechanically disrupt the cells.

Here, we demonstrated P-PDMS-PDA can support VBAM models with promising cellularity and myotube differentiation, however the vascular cells present in the model failed to form extensive microvessel networks when cultured with muscle cells (Fig 6). Instead, microvessel structures were limited to the VBAM surface. This may be due to competition from the densely seeded myoblasts, availability of nutrients, or the increased density of the culture following contraction. Incorporation of perfusion through the VBAM is a promising avenue to resolve nutrient diffusion issues, while providing mechanical signaling that supports microvessel formation [61,118,119].

A key advantage of the P-PDMS mold described in this work is the low cost and high accessibility, including the use of commercially available sugar cubes as a sacrificial template. There are drawbacks associated with sugar cube templating, such as fixed pore size based on the diameter of sugar granules, which cannot be readily tuned by the investigator. Should they be required, alternative fabrication strategies are available. P-PDMS can be formed via emulsion templating, phase separation, or use of sacrificial 3D printed templates [57,77,120]. These methods provide more flexibility in mold dimensions and porosity, but generally rely on complex fabrication techniques. Strategies to generate P-PDMS are thoroughly reviewed by Zhu and colleagues [121].

Additionally, we provide automated MATLAB algorithms that can be used to volumetrically quantify VBAM nuclei organization, alignment, and morphology in confocal microscopy data (S2 & S3 Files). Often, these parameters are quantified manually at pre-defined regions within 3D cell constructs, potentially concealing important spatial information. The described automated image analysis methods improve robustness by allowing for the entire 3D bulk to be analyzed and avoiding potential bias that may arise when manually selecting regions to quantify. Measurement of annular nuclear fraction provides further context into the distribution of cells within the tissue. Importantly, these algorithms can be implemented to assess nuclei organization and morphology in a broad range of engineered tissues.

VBAM maturation was further validated with PS-OCT. This imaging modality has previously been used to monitor collagen fiber alignment in engineered tendon constructs [122,123]. In this study, the presence of well aligned elongated myofibers in the MWF samples was evident from the phase retardation and orientation images which conforms with the immunostained images. The 3D vectorial birefringence images, which combine the information of the phase retardation and orientation, demonstrated highly organized and uniformly orientated muscle fibers throughout the volume of the MWF samples compared to the B.I.D samples. The quantitative comparison based on the phase retardation also exhibited improved differentiation in the MWF samples. All these results suggest that PS-OCT is a promising imaging modality for studying engineered tissue because it can non-invasively generate multi-modal 3D volumetric images and allow quantitative analysis without the use of any external agent.

Conclusion

We have demonstrated a novel culture molding technique capable of supporting contractile and metabolically active engineered tissues by varying S-PDMS surface functionalization and

increasing the surface area with P-PDMS molds. P-PDMS molds functionalized with PDA were shown to be suitable anchors for multiple 3D culture types and durations, including VBAMs. Overall, the fabrication methods described are readily extensible to research groups across a broad range of disciplines working on other contractile or metabolically active tissues such as fibrosis models, smooth muscle, and cardiac muscle.

References

1. Greek R, Menache A. Systematic Reviews of Animal Models: Methodology versus Epistemology. Int J Med Sci. 2013;10: 206–221. doi:10.7150/ijms.5529

2. Sutherland ML, Fabre KM, Tagle DA. The National Institutes of Health Microphysiological Systems Program focuses on a critical challenge in the drug discovery pipeline. Stem Cell Research & Therapy. 2013;4: I1. doi:10.1186/scrt361

3. Lipsky MS, Sharp LK. From idea to market: the drug approval process. J Am Board Fam Pract. 2001;14: 362–367.

4. Dyson A, Singer M. Animal models of sepsis: why does preclinical efficacy fail to translate to the clinical setting? Crit Care Med. 2009;37: S30-37. doi:10.1097/CCM.0b013e3181922bd3

5. Bédard P, Gauvin S, Ferland K, Caneparo C, Pellerin È, Chabaud S, et al. Innovative Human Three-Dimensional Tissue-Engineered Models as an Alternative to Animal Testing. Bioengineering. 2020;7: 115. doi:10.3390/bioengineering7030115

6. Bischoff H, Heller AH. Preclinical and clinical pharmacology of cerivastatin. The American Journal of Cardiology. 1998;82: 18J-25J. doi:10.1016/S0002-9149(98)00433-0

7. Bischoff H, Angerbauer R, Boberg M, Petzinna D, Schmidt D, Steinke W, et al. Preclinical review of cerivastatin sodium—a step forward in HMG-CoA reductase inhibition. Atherosclerosis. 1998;139: 7–13. doi:10.1016/S0021-9150(98)00188-9

8. Keutz E von, Schlüter G. Preclinical safety evaluation of cerivastatin, a novel HMG-CoA reductase inhibitor. The American Journal of Cardiology. 1998;82: 11J-17J. doi:10.1016/S0002-9149(98)00424-X

9. Thompson PD, Clarkson PM, Rosenson RS. An Assessment of Statin Safety by Muscle Experts. The American Journal of Cardiology. 2006;97: S69–S76. doi:10.1016/j.amjcard.2005.12.013

10. Gaukler SM, Ruff JS, Galland T, Underwood TK, Kandaris KA, Liu NM, et al. Quantification of cerivastatin toxicity supports organismal performance assays as an effective tool during pharmaceutical safety assessment. Evolutionary Applications. 2016;9: 685–696. doi:10.1111/eva.12365

11. Breslin S, O'Driscoll L. Three-dimensional cell culture: the missing link in drug discovery. Drug Discovery Today. 2013;18: 240–249. doi:10.1016/j.drudis.2012.10.003

12. Kapałczyńska M, Kolenda T, Przybyła W, Zajączkowska M, Teresiak A, Filas V, et al. 2D and 3D cell cultures - a comparison of different types of cancer cell cultures. Arch Med Sci. 2018;14: 910–919. doi:10.5114/aoms.2016.63743

13. Langhans SA. Three-Dimensional in Vitro Cell Culture Models in Drug Discovery and Drug Repositioning. Frontiers in Pharmacology. 2018;9. Available: https://www.frontiersin.org/articles/10.3389/fphar.2018.00006

14. Jensen C, Teng Y. Is It Time to Start Transitioning From 2D to 3D Cell Culture? Frontiers in Molecular Biosciences. 2020;7. Available: https://www.frontiersin.org/articles/10.3389/fmolb.2020.00033

15. Imamura Y, Mukohara T, Shimono Y, Funakoshi Y, Chayahara N, Toyoda M, et al. Comparison of 2D- and 3D-culture models as drug-testing platforms in breast cancer. Oncology Reports. 2015;33: 1837–1843. doi:10.3892/or.2015.3767

16. Soares CP, Midlej V, Oliveira MEW de, Benchimol M, Costa ML, Mermelstein C. 2D and 3D-Organized Cardiac Cells Shows Differences in Cellular Morphology, Adhesion Junctions, Presence of Myofibrils and Protein Expression. PLOS ONE. 2012;7: e38147. doi:10.1371/journal.pone.0038147

17. Ravi M, Paramesh V, Kaviya S r., Anuradha E, Solomon FDP. 3D Cell Culture Systems: Advantages and Applications. Journal of Cellular Physiology. 2015;230: 16–26. doi:10.1002/jcp.24683

18. Costa EC, Moreira AF, de Melo-Diogo D, Gaspar VM, Carvalho MP, Correia IJ. 3D tumor spheroids: an overview on the tools and techniques used for their analysis. Biotechnology Advances. 2016;34: 1427–1441. doi:10.1016/j.biotechadv.2016.11.002

19. Hu JL, Todhunter ME, LaBarge MA, Gartner ZJ. Opportunities for organoids as new models of aging. J Cell Biol. 2018;217: 39–50. doi:10.1083/jcb.201709054

20. Kosnik PE, Faulkner JA, Dennis RG. Functional Development of Engineered Skeletal Muscle from Adult and Neonatal Rats. Tissue Engineering. 2001;7: 573–584. doi:10.1089/107632701753213192

21. Machour M, Hen N, Goldfracht I, Safina D, Davidovich-Pinhas M, Bianco-Peled H, et al. Print-and-Grow within a Novel Support Material for 3D Bioprinting and Post-Printing Tissue Growth. Advanced Science. 2022;n/a: 2200882. doi:10.1002/advs.202200882

22. Ahearne M. Introduction to cell–hydrogel mechanosensing. Interface Focus. 2014;4: 20130038. doi:10.1098/rsfs.2013.0038

23. Gillette BM, Jensen JA, Tang B, Yang GJ, Bazargan-Lari A, Zhong M, et al. In situ collagen assembly for integrating microfabricated three-dimensional cell-seeded matrices. Nature Mater. 2008;7: 636–640. doi:10.1038/nmat2203

24. Brown XQ, Ookawa K, Wong JY. Evaluation of polydimethylsiloxane scaffolds with physiologically-relevant elastic moduli: interplay of substrate mechanics and surface chemistry effects on vascular smooth muscle cell response. Biomaterials. 2005;26: 3123–3129. doi:10.1016/j.biomaterials.2004.08.009

25. Chuah YJ, Koh YT, Lim K, Menon NV, Wu Y, Kang Y. Simple surface engineering of polydimethylsiloxane with polydopamine for stabilized mesenchymal stem cell adhesion and multipotency. Sci Rep. 2015;5: 18162. doi:10.1038/srep18162

26. Cross VL, Zheng Y, Won Choi N, Verbridge SS, Sutermaster BA, Bonassar LJ, et al. Dense type I collagen matrices that support cellular remodeling and microfabrication for studies of tumor angiogenesis and vasculogenesis in vitro. Biomaterials. 2010;31: 8596–8607. doi:10.1016/j.biomaterials.2010.07.072

27. Beauchamp RO, St Clair MBG, Fennell TR, Clarke DO, Morgan KT, Karl FW. A Critical Review of the Toxicology of Glutaraldehyde. Critical Reviews in Toxicology. 1992;22: 143–174. doi:10.3109/10408449209145322

28. Rideout K, Teschke K, Dimich-Ward H, Kennedy SM. Considering risks to healthcare workers from glutaraldehyde alternatives in high-level disinfection. Journal of Hospital Infection. 2005;59: 4–11. doi:10.1016/j.jhin.2004.07.003

29. Zeiger E, Gollapudi B, Spencer P. Genetic toxicity and carcinogenicity studies of glutaraldehyde—a review. Mutation Research/Reviews in Mutation Research. 2005;589: 136–151. doi:10.1016/j.mrrev.2005.01.001

30. Leung H-W. Ecotoxicology of Glutaraldehyde: Review of Environmental Fate and Effects Studies. Ecotoxicology and Environmental Safety. 2001;49: 26–39. doi:10.1006/eesa.2000.2031

31. Jolibois B, Guerbet M, Vassal S. Glutaraldehyde in Hospital Wastewater. Arch Environ Contam Toxicol. 2002;42: 137–144. doi:10.1007/s00244-001-0011-8

32. Morgan JT, Shirazi J, Comber EM, Eschenburg C, Gleghorn JP. Fabrication of centimeter-scale and geometrically arbitrary vascular networks using in vitro self-assembly. Biomaterials. 2019;189: 37–47. doi:10.1016/j.biomaterials.2018.10.021

33. Lee H, Dellatore SM, Miller WM, Messersmith PB. Mussel-Inspired Surface Chemistry for Multifunctional Coatings. Science. 2007;318: 426–430. doi:10.1126/science.1147241

34. Fu J, Quek KY, Chuah YJ, Lim CS, Fan C, Wang D. The effects of gelatin–dopamine coating on polydimethylsiloxane substrates on pluripotency maintenance and myocardial differentiation of cultured mouse embryonic stem cells. Journal of Materials Chemistry B. 2016;4: 7961–7973. doi:10.1039/C6TB02631A

35. Jeong S-Y, Lee J-H, Shin Y, Chung S, Kuh H-J. Co-Culture of Tumor Spheroids and Fibroblasts in a Collagen Matrix-Incorporated Microfluidic Chip Mimics Reciprocal

Activation in Solid Tumor Microenvironment. PLOS ONE. 2016;11: e0159013. doi:10.1371/journal.pone.0159013

36. Lee J-H, Kim S-K, Khawar IA, Jeong S-Y, Chung S, Kuh H-J. Microfluidic co-culture of pancreatic tumor spheroids with stellate cells as a novel 3D model for investigation of stroma-mediated cell motility and drug resistance. Journal of Experimental & Clinical Cancer Research. 2018;37: 4. doi:10.1186/s13046-017-0654-6

37. Harati J, Tao X, Shahsavarani H, Du P, Galluzzi M, Liu K, et al. Polydopamine-Mediated Protein Adsorption Alters the Epigenetic Status and Differentiation of Primary Human Adipose-Derived Stem Cells (hASCs). Front Bioeng Biotechnol. 2022;10: 934179. doi:10.3389/fbioe.2022.934179

38. Prasad BR, Brook MA, Smith T, Zhao S, Chen Y, Sheardown H, et al. Controlling cellular activity by manipulating silicone surface roughness. Colloids and Surfaces B: Biointerfaces. 2010;78: 237–242. doi:10.1016/j.colsurfb.2010.03.006

39. Juárez-Moreno JA, Ávila-Ortega A, Oliva AI, Avilés F, Cauich-Rodríguez JV. Effect of wettability and surface roughness on the adhesion properties of collagen on PDMS films treated by capacitively coupled oxygen plasma. Applied Surface Science. 2015;349: 763–773. doi:10.1016/j.apsusc.2015.05.063

40. Hwang Y, Seo D, Roy M, Han E, Candler RN, Seo S. Capillary Flow in PDMS Cylindrical Microfluidic Channel Using 3-D Printed Mold. Journal of Microelectromechanical Systems. 2016;25: 238–240. doi:10.1109/JMEMS.2016.2521858

41. Jang Y, Lee M, Kim H, Cha C, Jung J, Oh J. Comprehensive tuning of bioadhesive properties of polydimethylsiloxane (PDMS) membranes with controlled porosity. Biofabrication. 2019;11: 035021. doi:10.1088/1758-5090/ab1da9

42. Pedraza E, Brady A-C, Fraker CA, Molano RD, Sukert S, Berman DM, et al. Macroporous Three-Dimensional PDMS Scaffolds for Extrahepatic Islet Transplantation. Cell Transplant. 2013;22: 1123–1135. doi:10.3727/096368912X657440

43. Riesco R, Boyer L, Blosse S, Lefebvre PM, Assemat P, Leichle T, et al. Water-in-PDMS Emulsion Templating of Highly Interconnected Porous Architectures for 3D Cell Culture. ACS Appl Mater Interfaces. 2019;11: 28631–28640. doi:10.1021/acsami.9b07564

44. Varshney N, Sahi AK, Vajanthri KY, Poddar S, Balavigneswaran CK, Prabhakar A, et al. Culturing melanocytes and fibroblasts within three-dimensional macroporous PDMS scaffolds: towards skin dressing material. Cytotechnology. 2019;71: 287–303. doi:10.1007/s10616-018-0285-6

45. Vandenburgh HH, Karlisch P, Farr L. Maintenance of highly contractile tissue-cultured avian skeletal myotubes in collagen gel. In Vitro Cellular & Developmental Biology. 1988;24: 166–174. doi:10.1007/BF02623542

46. Vandenburgh H, Shansky J, Benesch- Lee F, Barbata V, Reid J, Thorrez L, et al. Drug-screening platform based on the contractility of tissue-engineered muscle. Muscle & Nerve. 2008;37: 438–447. doi:10.1002/mus.20931

47. Bian W, Bursac N. Engineered skeletal muscle tissue networks with controllable architecture. Biomaterials. 2009;30: 1401–1412. doi:10.1016/j.biomaterials.2008.11.015

48. Iuliano A, van der Wal E, Ruijmbeek CWB, in 't Groen SLM, Pijnappel WWMP, de Greef JC, et al. Coupling 3D Printing and Novel Replica Molding for In House Fabrication of Skeletal Muscle Tissue Engineering Devices. Advanced Materials Technologies. 2020;5: 2000344. doi:10.1002/admt.202000344

49. Capel AJ, Rimington RP, Fleming JW, Player DJ, Baker LA, Turner MC, et al. Scalable 3D Printed Molds for Human Tissue Engineered Skeletal Muscle. Front Bioeng Biotechnol. 2019;7. doi:10.3389/fbioe.2019.00020

50. Christensen RK, von Halling Laier C, Kiziltay A, Wilson S, Larsen NB. 3D Printed Hydrogel Multiassay Platforms for Robust Generation of Engineered Contractile Tissues. Biomacromolecules. 2020;21: 356–365. doi:10.1021/acs.biomac.9b01274

51. Mudera V, Smith A s. t., Brady M a., Lewis M p. The effect of cell density on the maturation and contractile ability of muscle derived cells in a 3D tissue-engineered skeletal muscle model and determination of the cellular and mechanical stimuli required for the synthesis of a postural phenotype. Journal of Cellular Physiology. 2010;225: 646–653. doi:10.1002/jcp.22271

52. Wragg NM, Player DJ, Martin NRW, Liu Y, Lewis MP. Development of tissue-engineered skeletal muscle manufacturing variables. Biotechnology and Bioengineering. 2019;116: 2364–2376. doi:10.1002/bit.27074

53. Gefen A, Cornelissen LH, Gawlitta D, Bader DL, Oomens CWJ. The free diffusion of macromolecules in tissue-engineered skeletal muscle subjected to large compression strains. Journal of Biomechanics. 2008;41: 845–853. doi:10.1016/j.jbiomech.2007.10.023

54. Hinds S, Bian W, Dennis RG, Bursac N. The Role of Extracellular Matrix Composition in Structure and Function of Bioengineered Skeletal Muscle. Biomaterials. 2011;32: 3575–3583. doi:10.1016/j.biomaterials.2011.01.062

55. van der Schaft DWJ, van Spreeuwel ACC, Boonen KJM, Langelaan MLP, Bouten CVC, Baaijens FPT. Engineering Skeletal Muscle Tissues from Murine Myoblast Progenitor Cells and Application of Electrical Stimulation. J Vis Exp. 2013; 4267. doi:10.3791/4267

56. Dennis RG, Kosnik PE. Excitability and isometric contractile properties of mammalian skeletal muscle constructs engineered in vitro. In Vitro CellDevBiol-Animal. 2000;36: 327–335. doi:10.1290/1071-2690(2000)036<0327:EAICPO>2.0.CO;2

57. Huang Y-C, Dennis RG, Larkin L, Baar K. Rapid formation of functional muscle in vitro using fibrin gels. Journal of Applied Physiology. 2005;98: 706–713. doi:10.1152/japplphysiol.00273.2004

58. Smith AST, Passey S, Greensmith L, Mudera V, Lewis MP. Characterization and optimization of a simple, repeatable system for the long term in vitro culture of aligned myotubes in 3D. Journal of Cellular Biochemistry. 2012;113: 1044–1053. doi:10.1002/jcb.23437

59. Alave Reyes-Furrer A, De Andrade S, Bachmann D, Jeker H, Steinmann M, Accart N, et al. Matrigel 3D bioprinting of contractile human skeletal muscle models recapitulating exercise and pharmacological responses. Commun Biol. 2021;4: 1–12. doi:10.1038/s42003-021-02691-0

60. Griffith LG, Swartz MA. Capturing complex 3D tissue physiology in vitro. Nature Reviews Molecular Cell Biology. 2006;7: 211–224. doi:10.1038/nrm1858

61. Zohar B, Blinder Y, Mooney DJ, Levenberg S. Flow-Induced Vascular Network Formation and Maturation in Three-Dimensional Engineered Tissue. ACS Biomater Sci Eng. 2018;4: 1265–1271. doi:10.1021/acsbiomaterials.7b00025

62. Buchwald P. FEM-based oxygen consumption and cell viability models for avascular pancreatic islets. Theoretical Biology and Medical Modelling. 2009;6: 5. doi:10.1186/1742-4682-6-5

63. Enrico A, Voulgaris D, Östmans R, Sundaravadivel N, Moutaux L, Cordier A, et al. 3D Microvascularized Tissue Models by Laser-Based Cavitation Molding of Collagen. Advanced Materials. 2022;34: 2109823. doi:10.1002/adma.202109823

64. Karande TS, Ong JL, Agrawal CM. Diffusion in Musculoskeletal Tissue Engineering Scaffolds: Design Issues Related to Porosity, Permeability, Architecture, and Nutrient Mixing. Ann Biomed Eng. 2004;32: 1728–1743. doi:10.1007/s10439-004-7825-2

65. van der Valk J, Brunner D, De Smet K, Fex Svenningsen Å, Honegger P, Knudsen LE, et al. Optimization of chemically defined cell culture media – Replacing fetal bovine serum in mammalian in vitro methods. Toxicology in Vitro. 2010;24: 1053–1063. doi:10.1016/j.tiv.2010.03.016

66. Quiroga-Campano AL, Panoskaltsis N, Mantalaris A. Energy-based culture medium design for biomanufacturing optimization: A case study in monoclonal antibody production by GS-NS0 cells. Metabolic Engineering. 2018;47: 21–30. doi:10.1016/j.ymben.2018.02.013

67. Bancroft GN, Sikavitsas VI, van den Dolder J, Sheffield TL, Ambrose CG, Jansen JA, et al. Fluid flow increases mineralized matrix deposition in 3D perfusion culture of marrow stromal osteoblasts in a dose-dependent manner. Proc Natl Acad Sci USA. 2002;99: 12600–12605. doi:10.1073/pnas.202296599

68. Sikavitsas VI, Bancroft GN, Lemoine JJ, Liebschner MAK, Dauner M, Mikos AG. Flow Perfusion Enhances the Calcified Matrix Deposition of Marrow Stromal Cells in Biodegradable Nonwoven Fiber Mesh Scaffolds. Ann Biomed Eng. 2005;33: 63–70. doi:10.1007/s10439-005-8963-x

69. Grayson WL, Bhumiratana S, Cannizzaro C, Chao P-HG, Lennon DP, Caplan AI, et al. Effects of Initial Seeding Density and Fluid Perfusion Rate on Formation of Tissue-Engineered Bone. Tissue Engineering Part A. 2008;14: 1809–1820. doi:10.1089/ten.tea.2007.0255

70. Pazzano D, Mercier KA, Moran JM, Fong SS, DiBiasio DD, Rulfs JX, et al. Comparison of Chondrogensis in Static and Perfused Bioreactor Culture. Biotechnol Prog. 2000;16: 893–896. doi:10.1021/bp000082v

71. Davisson T, Sah RL, Ratcliffe A. Perfusion Increases Cell Content and Matrix Synthesis in Chondrocyte Three-Dimensional Cultures. Tissue Engineering. 2002;8: 807–816. doi:10.1089/10763270260424169

72. Vollert I, Seiffert M, Bachmair J, Sander M, Eder A, Conradi L, et al. In Vitro Perfusion of Engineered Heart Tissue Through Endothelialized Channels. Tissue Engineering Part A. 2013;20: 854–863. doi:10.1089/ten.tea.2013.0214

73. Kim H, Osaki T, Kamm RD, Asada HH. Multiscale engineered human skeletal muscles with perfusable vasculature and microvascular network recapitulating the fluid compartments. Biofabrication. 2022;15: 015005. doi:10.1088/1758-5090/ac933d

74. Martin I, Wendt D, Heberer M. The role of bioreactors in tissue engineering. Trends in Biotechnology. 2004;22: 80–86. doi:10.1016/j.tibtech.2003.12.001

75. Li Z, Cui Z. Three-dimensional perfused cell culture. Biotechnology Advances. 2014;32: 243–254. doi:10.1016/j.biotechadv.2013.10.006

76. Gelinsky M, Bernhardt A, Milan F. Bioreactors in tissue engineering: Advances in stem cell culture and three-dimensional tissue constructs. Engineering in Life Sciences. 2015;15: 670–677. doi:10.1002/elsc.201400216

77. Thurgood P, Baratchi S, Szydzik C, Mitchell A, Khoshmanesh K. Porous PDMS structures for the storage and release of aqueous solutions into fluidic environments. Lab on a Chip. 2017;17: 2517–2527. doi:10.1039/C7LC00350A

78. Yu C, Yu C, Cui L, Song Z, Zhao X, Ma Y, et al. Facile Preparation of the Porous PDMS Oil-Absorbent for Oil/Water Separation. Advanced Materials Interfaces. 2017;4: 1600862. doi:10.1002/admi.201600862

79. Zhang L, Zhang Y, Chen P, Du W, Feng X, Liu B-F. Paraffin Oil Based Soft-Template Approach to Fabricate Reusable Porous PDMS Sponge for Effective Oil/Water Separation. Langmuir. 2019;35: 11123–11131. doi:10.1021/acs.langmuir.9b01861

80. Rajan N, Habermehl J, Coté M-F, Doillon CJ, Mantovani D. Preparation of ready-to-use, storable and reconstituted type I collagen from rat tail tendon for tissue engineering applications. Nat Protoc. 2006;1: 2753–2758. doi:10.1038/nprot.2006.430

81. García-Gareta E. Collagen gels and the "Bornstein legacy": from a substrate for tissue culture to cell culture systems and biomaterials for tissue regeneration. Exp Dermatol. 2014;23: 473–474. doi:10.1111/exd.12404

82. Ren X, Lu H, Zhou JG, Chong PL-G, Yuan W, Noh M. Porous Polydimethylsiloxane as a Gas–Liquid Interface for Microfluidic Applications. Journal of Microelectromechanical Systems. 2017;26: 120–126. doi:10.1109/JMEMS.2016.2618395

83. González-Rivera J, Iglio R, Barillaro G, Duce C, Tinè MR. Structural and Thermoanalytical Characterization of 3D Porous PDMS Foam Materials: The Effect of Impurities Derived from a Sugar Templating Process. Polymers. 2018;10: 616. doi:10.3390/polym10060616

84. Li Q, Duan T, Shao J, Yu H. Fabrication method for structured porous polydimethylsiloxane (PDMS). J Mater Sci. 2018;53: 11873–11882. doi:10.1007/s10853-018-2396-z

85. Chen RR, Silva EA, Yuen WW, Mooney DJ. Spatio–temporal VEGF and PDGF Delivery Patterns Blood Vessel Formation and Maturation. Pharm Res. 2007;24: 258–264. doi:10.1007/s11095-006-9173-4

86. Han F, Jia X, Dai D, Yang X, Zhao J, Zhao Y, et al. Performance of a multilayered small-diameter vascular scaffold dual-loaded with VEGF and PDGF. Biomaterials. 2013;34: 7302–7313. doi:10.1016/j.biomaterials.2013.06.006

87. Dent JA, Polson AG, Klymkowsky MW. A whole-mount immunocytochemical analysis of the expression of the intermediate filament protein vimentin in Xenopus. Development. 1989;105: 61–74. doi:10.1242/dev.105.1.61

88. Ahnfelt-Rønne J, Jørgensen MC, Hald J, Madsen OD, Serup P, Hecksher-Sørensen J. An Improved Method for Three-dimensional Reconstruction of Protein Expression Patterns in Intact Mouse and Chicken Embryos and Organs. J Histochem Cytochem. 2007;55: 925–930. doi:10.1369/jhc.7A7226.2007

89. Sanchez MM, Morgan JT. Generation of Self-assembled Vascularized Human Skin Equivalents. JoVE. 2021; e62125. doi:10.3791/62125

90. Preibisch S, Saalfeld S, Tomancak P. Globally optimal stitching of tiled 3D microscopic image acquisitions. Bioinformatics. 2009;25: 1463–1465. doi:10.1093/bioinformatics/btp184

91. Van Uitert R, Bitter I. Subvoxel precise skeletons of volumetric data based on fast marching methods. Medical Physics. 2007;34: 627–638. doi:10.1118/1.2409238

92. Shirazi J, Morgan JT, Comber EM, Gleghorn JP. Generation and morphological quantification of large scale, three-dimensional, self-assembled vascular networks. MethodsX. 2019;6: 1907–1918. doi:10.1016/j.mex.2019.08.006

93. Wang Y, Oh CM, Oliveira MC, Islam MS, Ortega A, Park BH. GPU accelerated real-time multi-functional spectral-domain optical coherence tomography system at 1300nm. Opt Express, OE. 2012;20: 14797–14813. doi:10.1364/OE.20.014797

94. Mitsui T. Dynamic Range of Optical Reflectometry with Spectral Interferometry. Jpn J Appl Phys. 1999;38: 6133. doi:10.1143/JJAP.38.6133

95. Wojtkowski M, Leitgeb R, Kowalczyk A, Bajraszewski T, Fercher AF. In vivo human retinal imaging by Fourier domain optical coherence tomography. J Biomed Opt. 2002;7: 457. doi:10.1117/1.1482379

96. Choma M, Sarunic M, Yang C, Izatt J. Sensitivity advantage of swept source and Fourier domain optical coherence tomography. Opt Express. 2003;11: 2183. doi:10.1364/OE.11.002183

97. de Boer JF, Cense B, Park BH, Pierce MC, Tearney GJ, Bouma BE. Improved signal-to-noise ratio in spectral-domain compared with time-domain optical coherence tomography. Opt Lett. 2003;28: 2067. doi:10.1364/OL.28.002067

98. Nassif N, Cense B, Hyle Park B, Yun SH, Chen TC, Bouma BE, et al. In vivo human retinal imaging by ultrahigh-speed spectral domain optical coherence tomography. Opt Lett. 2004;29: 480. doi:10.1364/OL.29.000480

99. Haskell RC, Carlson FD, Blank PS. Form birefringence of muscle. Biophysical Journal. 1989;56: 401–413. doi:10.1016/S0006-3495(89)82686-4

100. Hee MR, Huang D, Swanson EA, Fujimoto JG. Polarization-sensitive low-coherence reflectometer for birefringence characterization and ranging. J Opt Soc Am B, JOSAB. 1992;9: 903–908. doi:10.1364/JOSAB.9.000903

101. de Boer JF, Milner TE, Van Gemert MJC, Nelson JS. Two-dimensional birefringence imaging in biological tissue by polarization-sensitive optical coherence tomography. Opt Lett. 1997;22: 934. doi:10.1364/OL.22.000934

102. Park BH, Saxer C, Srinivas SM, Nelson JS, de Boer JF. In vivo burn depth determination by high-speed fiber-based polarization sensitive optical coherence tomography. J Biomed Opt. 2001;6: 474. doi:10.1117/1.1413208

103. Park BH, Pierce MC, Cense B, de Boer JF. Optic axis determination accuracy for fiber-based polarization-sensitive optical coherence tomography. Opt Lett. 2005;30: 2587. doi:10.1364/OL.30.002587

104. Villiger M, Zhang EZ, Nadkarni SK, Oh W-Y, Vakoc BJ, Bouma BE. Spectral binning for mitigation of polarization mode dispersion artifacts in catheter-based optical frequency domain imaging. Opt Express. 2013;21: 16353. doi:10.1364/OE.21.016353

105. Nam AS, Easow JM, Chico-Calero I, Villiger M, Welt J, Borschel GH, et al. Wide-Field Functional Microscopy of Peripheral Nerve Injury and Regeneration. Sci Rep. 2018;8: 14004. doi:10.1038/s41598-018-32346-w

106. Selman Sakar M, Neal D, Boudou T, A. Borochin M, Li Y, Weiss R, et al. Formation and optogenetic control of engineered 3D skeletal muscle bioactuators. Lab on a Chip. 2012;12: 4976–4985. doi:10.1039/C2LC40338B

107. Duffy RM, Feinberg AW. Engineered skeletal muscle tissue for soft robotics: fabrication strategies, current applications, and future challenges. Wiley Interdisciplinary Reviews: Nanomedicine and Nanobiotechnology. 2014;6: 178–195. doi:10.1002/wnan.1254

108. Mueller C, Trujillo-Miranda M, Maier M, Heath DE, O'Connor AJ, Salehi S. Effects of External Stimulators on Engineered Skeletal Muscle Tissue Maturation. Advanced Materials Interfaces. 2021;8: 2001167. doi:10.1002/admi.202001167

109. Ariyasinghe NR, Santoso JW, Gupta D, Pincus MJ, August PR, McCain ML. Optical Clearing of Skeletal Muscle Bundles Engineered in 3-D Printed Templates. Ann Biomed Eng. 2021;49: 523–535. doi:10.1007/s10439-020-02583-0

110. Brancato V, Oliveira JM, Correlo VM, Reis RL, Kundu SC. Could 3D models of cancer enhance drug screening? Biomaterials. 2020;232: 119744. doi:10.1016/j.biomaterials.2019.119744

111. King MG, Baragwanath AJ, Rosamond MC, Wood D, Gallant AJ. Porous PDMS force sensitive resistors. Procedia Chemistry. 2009;1: 568–571. doi:10.1016/j.proche.2009.07.142

112. Park E, Hur J. Three-dimensionally interconnected porous PDMS decorated with poly(dopamine) and Prussian blue for floatable, flexible, and recyclable photo-Fenton catalyst activated by solar light. Applied Surface Science. 2021;545: 148990. doi:10.1016/j.apsusc.2021.148990

113. Díaz Lantada A, Alarcón Iniesta H, Pareja Sánchez B, García-Ruíz JP. Free-Form Rapid Prototyped Porous PDMS Scaffolds Incorporating Growth Factors Promote Chondrogenesis. Advances in Materials Science and Engineering. 2014;2014: e612976. doi:10.1155/2014/612976

114. Si J, Cui Z, Xie P, Song L, Wang Q, Liu Q, et al. Characterization of 3D elastic porous polydimethylsiloxane (PDMS) cell scaffolds fabricated by VARTM and particle leaching. Journal of Applied Polymer Science. 2016;133. doi:10.1002/app.42909

115. Zargar R, Nourmohammadi J, Amoabediny G. Preparation, characterization, and silanization of 3D microporous PDMS structure with properly sized pores for endothelial

cell culture. Biotechnology and Applied Biochemistry. 2016;63: 190–199. doi:10.1002/bab.1371

116. Quirós-Solano WF, Gaio N, Stassen OMJA, Arik YB, Silvestri C, Van Engeland NCA, et al. Microfabricated tuneable and transferable porous PDMS membranes for Organs-on-Chips. Sci Rep. 2018;8: 13524. doi:10.1038/s41598-018-31912-6

117. Cooper ST, Maxwell AL, Kizana E, Ghoddusi M, Hardeman EC, Alexander IE, et al. C2C12 Co-culture on a fibroblast substratum enables sustained survival of contractile, highly differentiated myotubes with peripheral nuclei and adult fast myosin expression. Cell Motility. 2004;58: 200–211. doi:10.1002/cm.20010

118. Galie PA, Nguyen D-HT, Choi CK, Cohen DM, Janmey PA, Chen CS. Fluid shear stress threshold regulates angiogenic sprouting. Proceedings of the National Academy of Sciences. 2014;111: 7968–7973. doi:10.1073/pnas.1310842111

119. Kinstlinger IS, Calderon GA, Royse MK, Means AK, Grigoryan B, Miller JS. Perfusion and endothelialization of engineered tissues with patterned vascular networks. Nat Protoc. 2021; 1–25. doi:10.1038/s41596-021-00533-1

120. Montazerian H, Mohamed MGA, Mohaghegh Montazeri M, Kheiri S, Milani AS, Kim K, et al. Permeability and mechanical properties of gradient porous PDMS scaffolds fabricated by 3D-printed sacrificial templates designed with minimal surfaces. Acta Biomaterialia. 2019 [cited 1 Jul 2019]. doi:10.1016/j.actbio.2019.06.040

121. Zhu D, Handschuh-Wang S, Zhou X. Recent progress in fabrication and application of polydimethylsiloxane sponges. Journal of Materials Chemistry A. 2017;5: 16467–16497. doi:10.1039/C7TA04577H

122. Ahearne M, Bagnaninchi PO, Yang Y, El Haj AJ. Online monitoring of collagen fibre alignment in tissue-engineered tendon by PSOCT. Journal of Tissue Engineering and Regenerative Medicine. 2008;2: 521–524. doi:10.1002/term.124

123. Yang Y, Ahearne M, Wimpenny I, Guijarro-Leach J, Torbet J. Investigation of a tissue engineered tendon model by PS-OCT. In: Kirkpatrick SJ, Wang R, editors. San Francisco, California; 2010. p. 75660A. doi:10.1117/12.842302

Supporting information

S1 Table. Media formulations. Composition of media blends that are used for cell culture.

S2 Table. Antibody staining reagents. A summary of primary and secondary antibodies used for 3D cell culture staining.

S1 File. Supplementary materials and methods. Extended experimental procedures.

S2 File. MATLAB code for VBAM annular nuclear fraction quantification and nuclear aspect ratio.

S3 File. MATLAB code for VBAM nuclear alignment.

S1 Fig. VBAM differentiation media supports vascular network formation in EC/ASC co-culture. ECs and ASCs were cultured in VBAM differentiation media with VEGF (weeks 0-2) or PDGF-BB (weeks 2-4) before being fixed and stained against collagen IV (EC basement membrane marker). Shown is a depth-coded projection of a stitched tilescan demonstrating vascular networks have assembled and are present through the culture bulk (scalebar = 250 μm).

S2 Fig. (A) **The average phase retardation as a function of sample length for the MWF and B.I.D samples.** The whole length of the B.I.D2 sample could not be obtained because of the pins used to fix the samples during imaging. (B-C) Representative en face phase retardation images (in rad/mm) taken from the middle of the MWF1 and BID1, respectively (scalebar = 1 mm). The MWF samples have higher phase retardation throughout the length of the samples compared to the B.I.D samples.

S3 Fig. 3D renderings of segmented nuclei of S-PDMS and P-PDMS cultures maintained via side wall diffusion. Stitched tilescans were rendered in 3D to visualize spatial distribution of nuclei. Density of P-PDMS nuclei appears increased with evidence of dense aggregate formation relative to S-PDMS.

S4 Fig. 3D renderings of segmented nuclei in stitched tilescans of MWF and B.I.D Morph #1 (3 mm x 1 mm x 0.6 mm). Nuclei density is increased with consistent organization globally in MWF VBAMs.

S5 Fig. Effects of daily feeding on VBAM cellularity. (A) Representative transverse projection of VBAM nuclei after 5 weeks of daily media changes show similar nuclei density to MWF samples. (B) 3D rendering of segmented nuclei of daily fed VBAM indicate similar spatial organization of the nuclei to MWF samples.

Figure 1

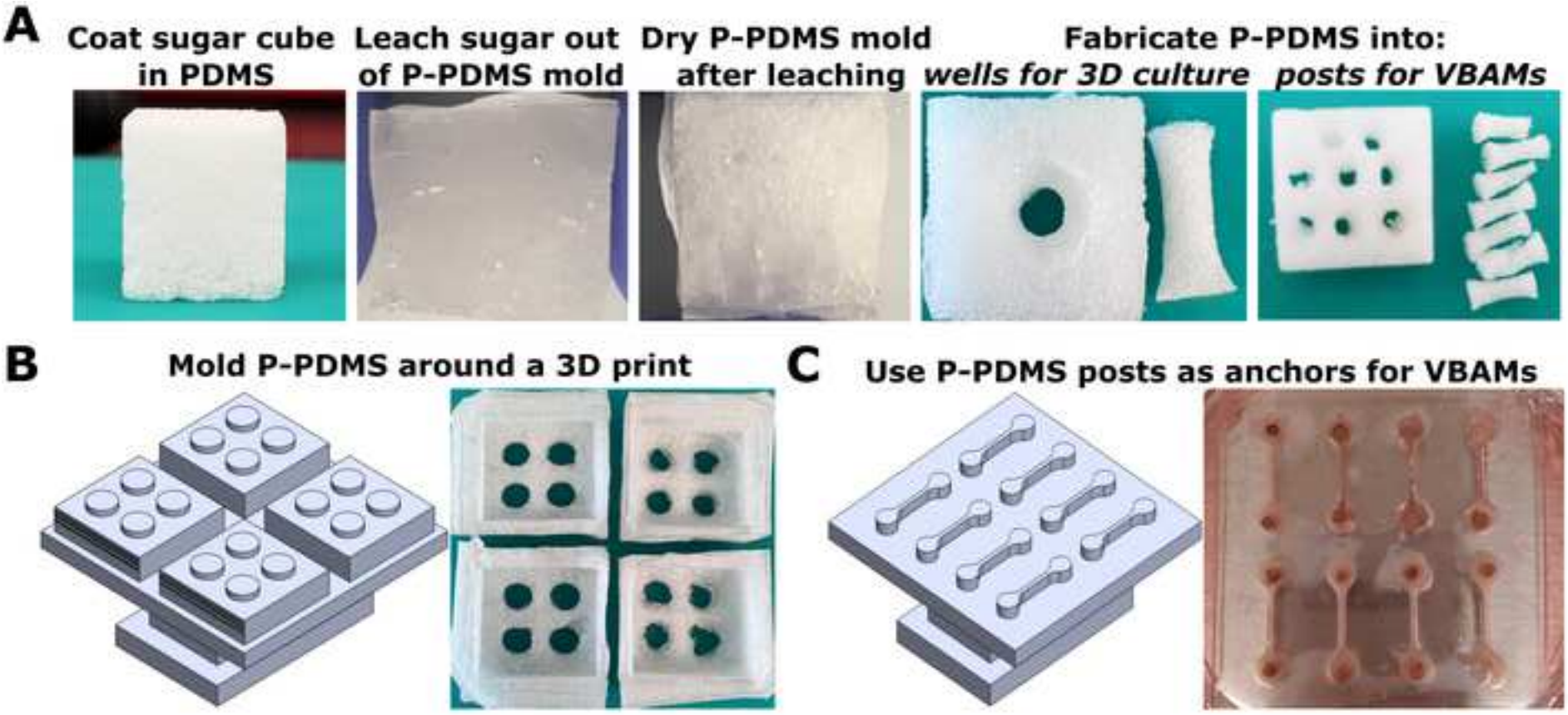
A
Coat sugar cube in PDMS
Leach sugar out of P-PDMS mold
Dry P-PDMS mold after leaching
Fabricate P-PDMS into:
wells for 3D culture
posts for VBAMs
B
Mold P-PDMS around a 3D print
C
Use P-PDMS posts as anchors for VBAMs

Figure 2

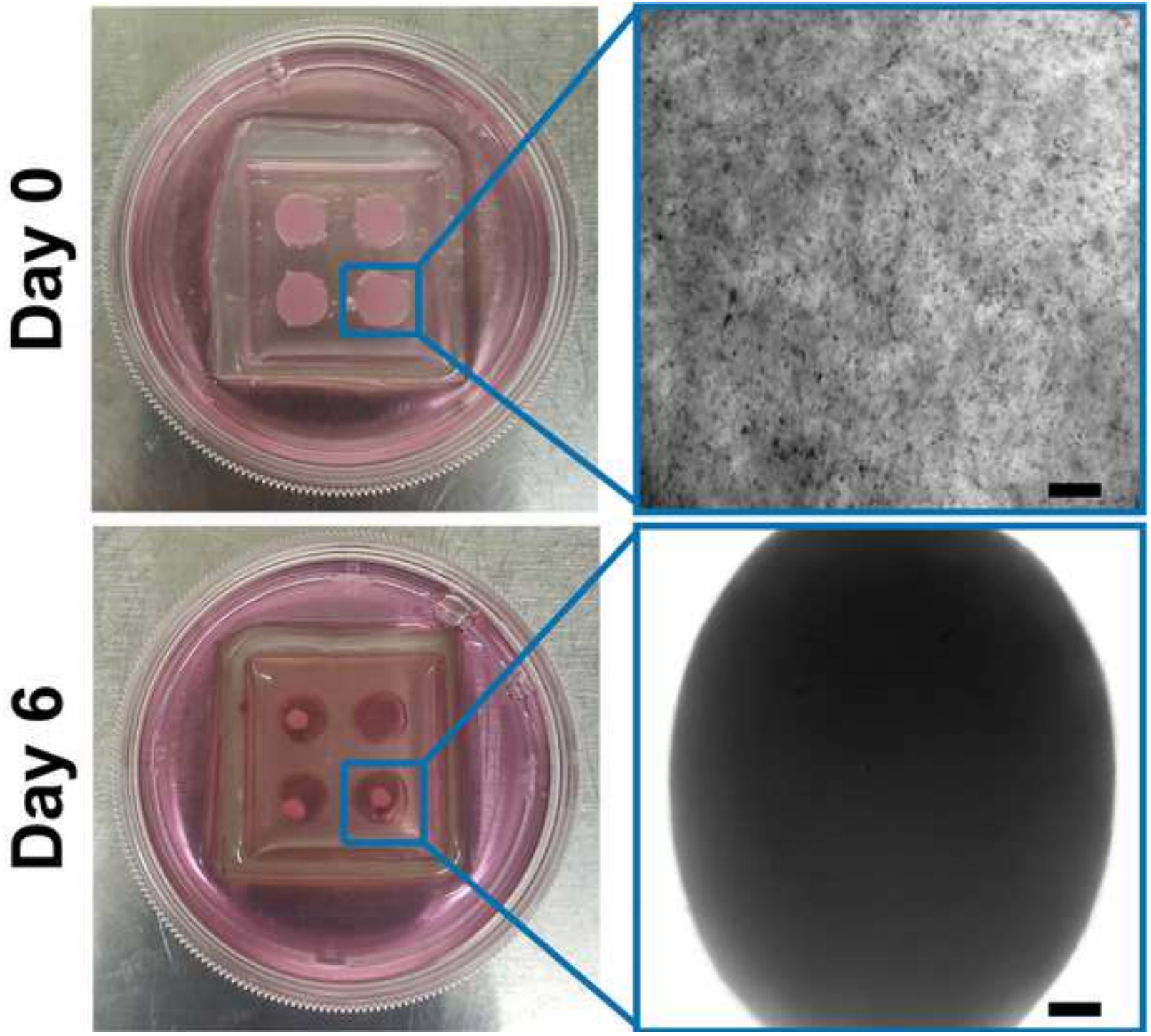

Figure 3


Transverse
100 μm
Distance Transform
150
100
50
0
distance (μm)
Annular Rings

Figure 4

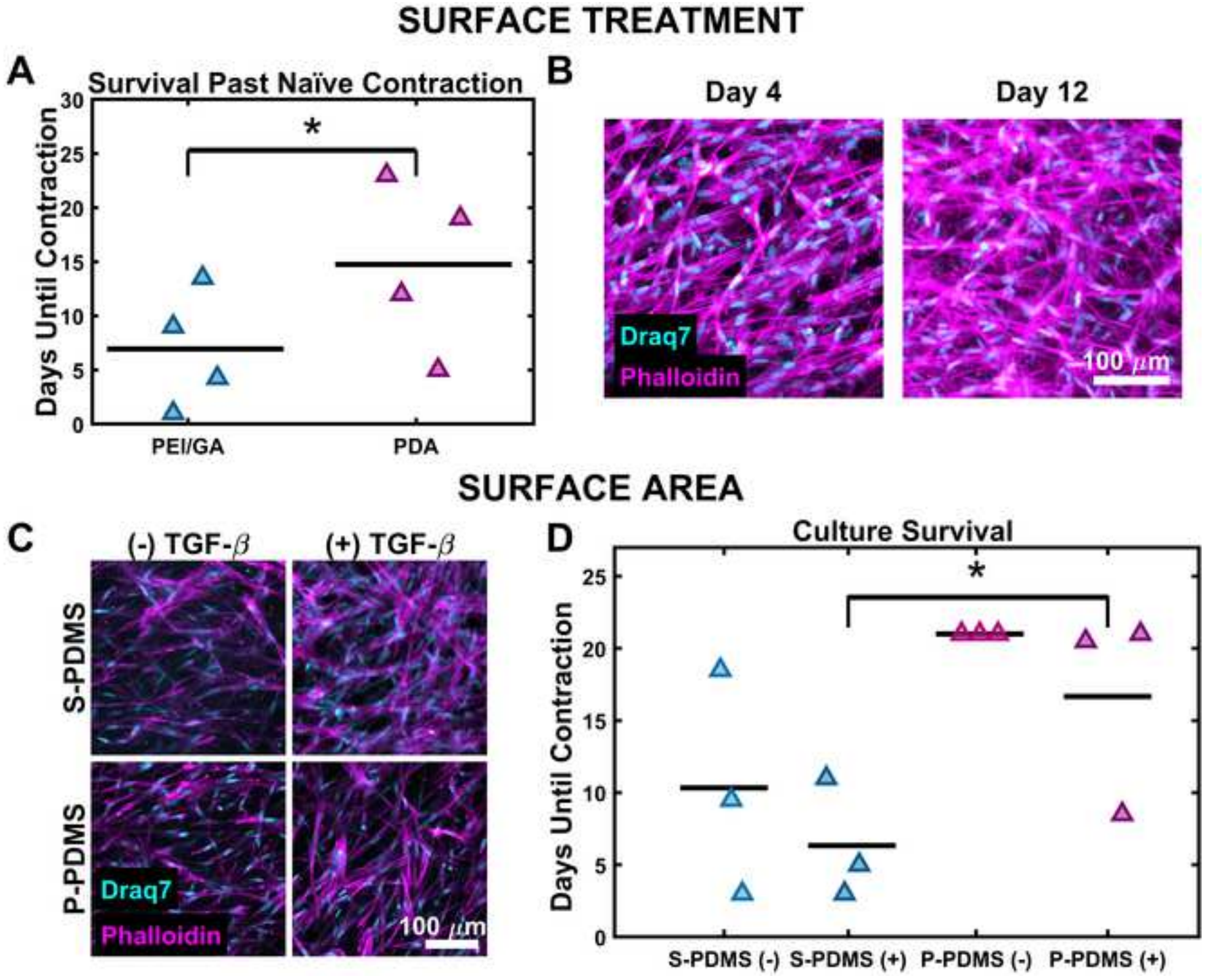
SURFACE TREATMENT
A
Survival Past Naïve Contraction
Days Until Contraction
30
25
20
15
10
5
0
*
PEI/GA
PDA
B
Day 4
Day 12
Draq7
Phalloidin
100 μm
SURFACE AREA
C
(-) TGF-β
(+) TGF-β
S-PDMS
P-PDMS
Draq7
Phalloidin
100 μm
D
Culture Survival
Days Until Contraction
25
20
15
10
5
0
*
S-PDMS (-)
S-PDMS (+)
P-PDMS (-)
P-PDMS (+)

Figure 5

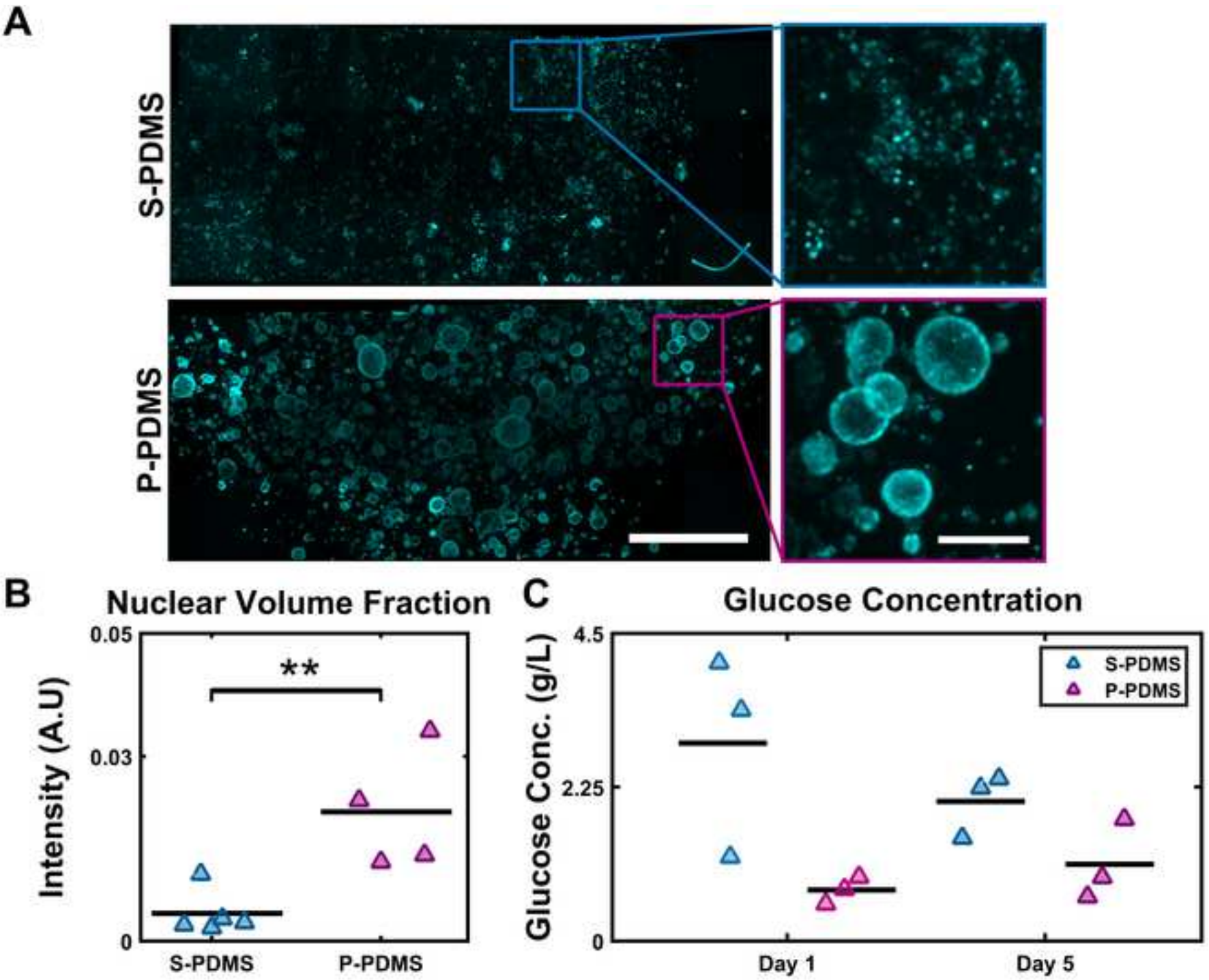
A
S-PDMS
P-PDMS
B
Nuclear Volume Fraction
Intensity (A.U)
0.05
0.03
0
**
S-PDMS
P-PDMS
C
Glucose Concentration
Glucose Conc. (g/L)
4.5
2.25
0
S-PDMS
P-PDMS
Day 1
Day 5

Figure 6

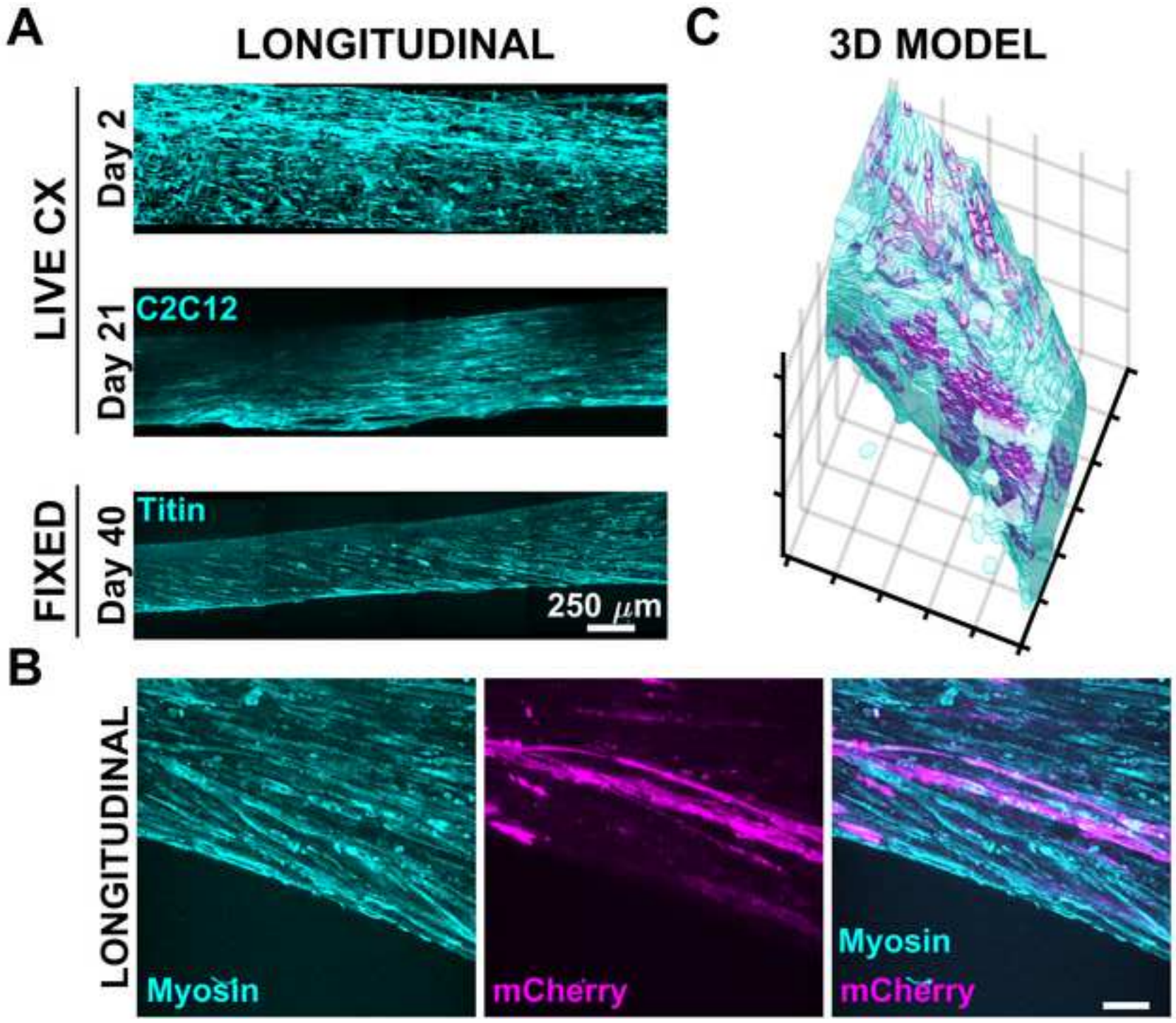
A
LONGITUDINAL
LIVE CX
Day 2
Day 21
C2C12
FIXED
Day 40
Titin
250 μm
C
3D MODEL
B
LONGITUDINAL
Myosin
mCherry
Myosin
mCherry

Figure 7

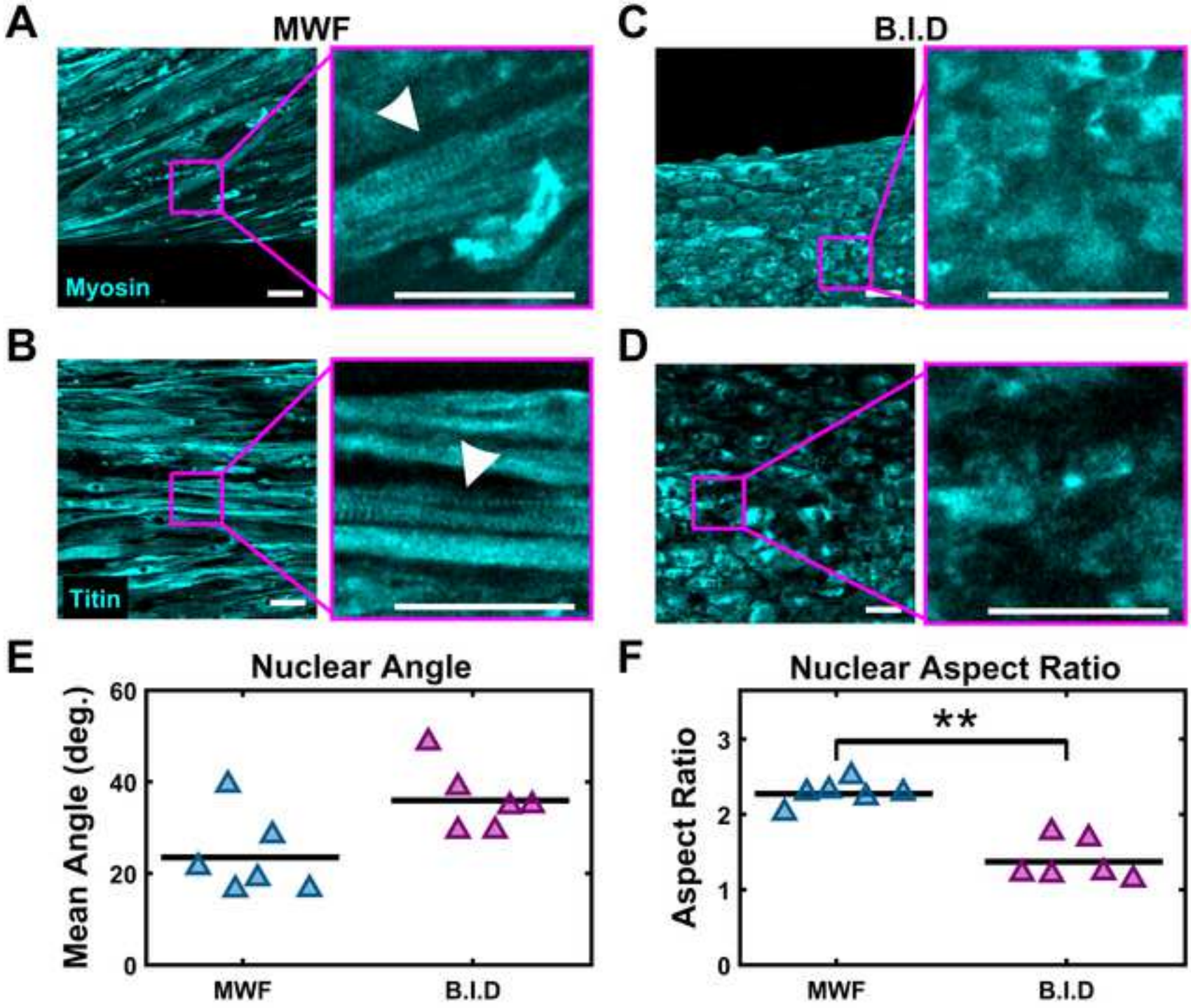
A
MWF
Myosin
C
B.I.D
B
Titin
D
E
Nuclear Angle
Mean Angle (deg.)
60
40
20
0
MWF
B.I.D
F
Nuclear Aspect Ratio
**
Aspect Ratio
3
2
1
0
MWF
B.I.D

Figure 8

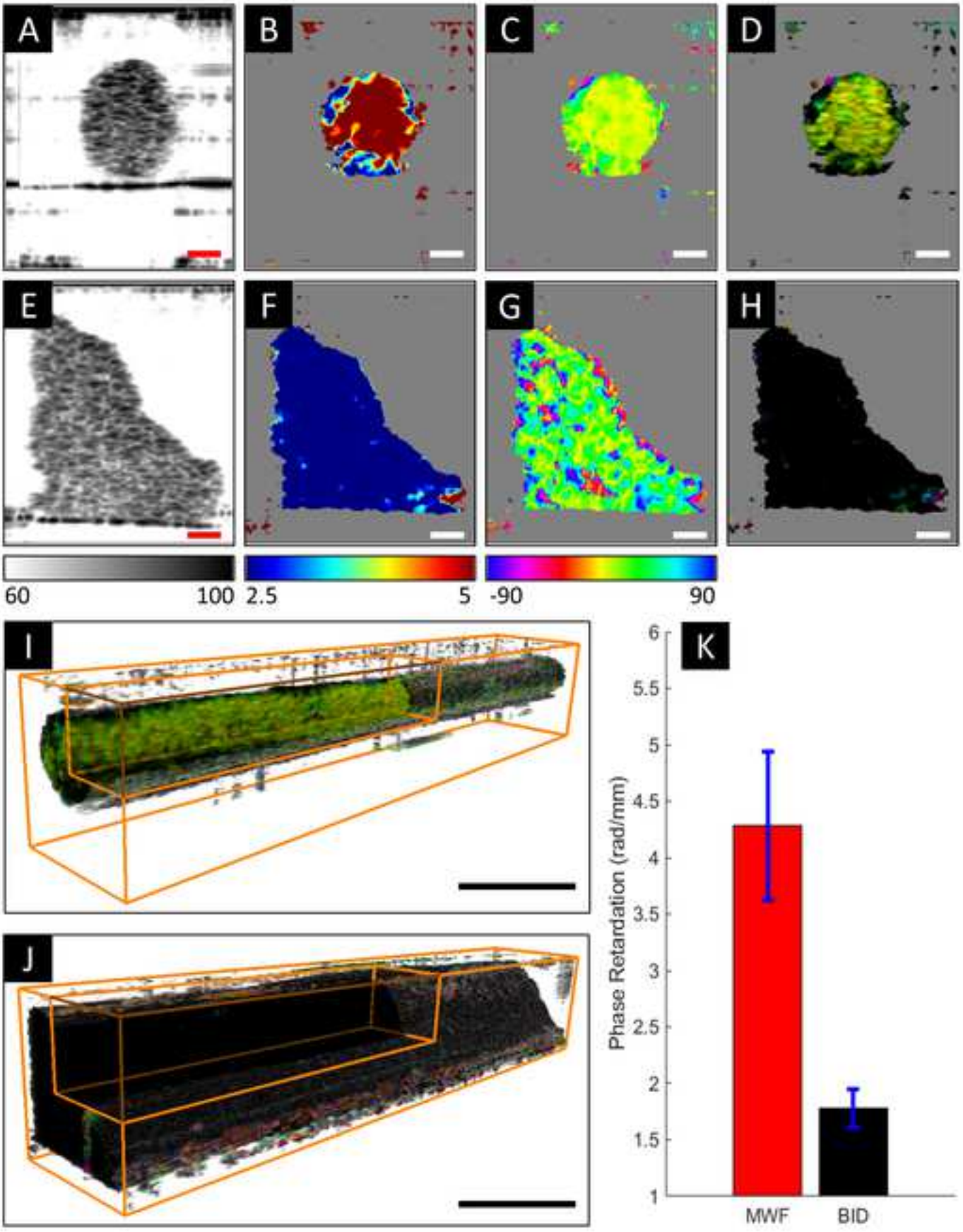
A
B
C
D
E
F
G
H
60
100
2.5
5
-90
90
I
J
K
Phase Retardation (rad/mm)
6
5.5
5
4.5
4
3.5
3
2.5
2
1.5
1
MWF
BID

Figure 9

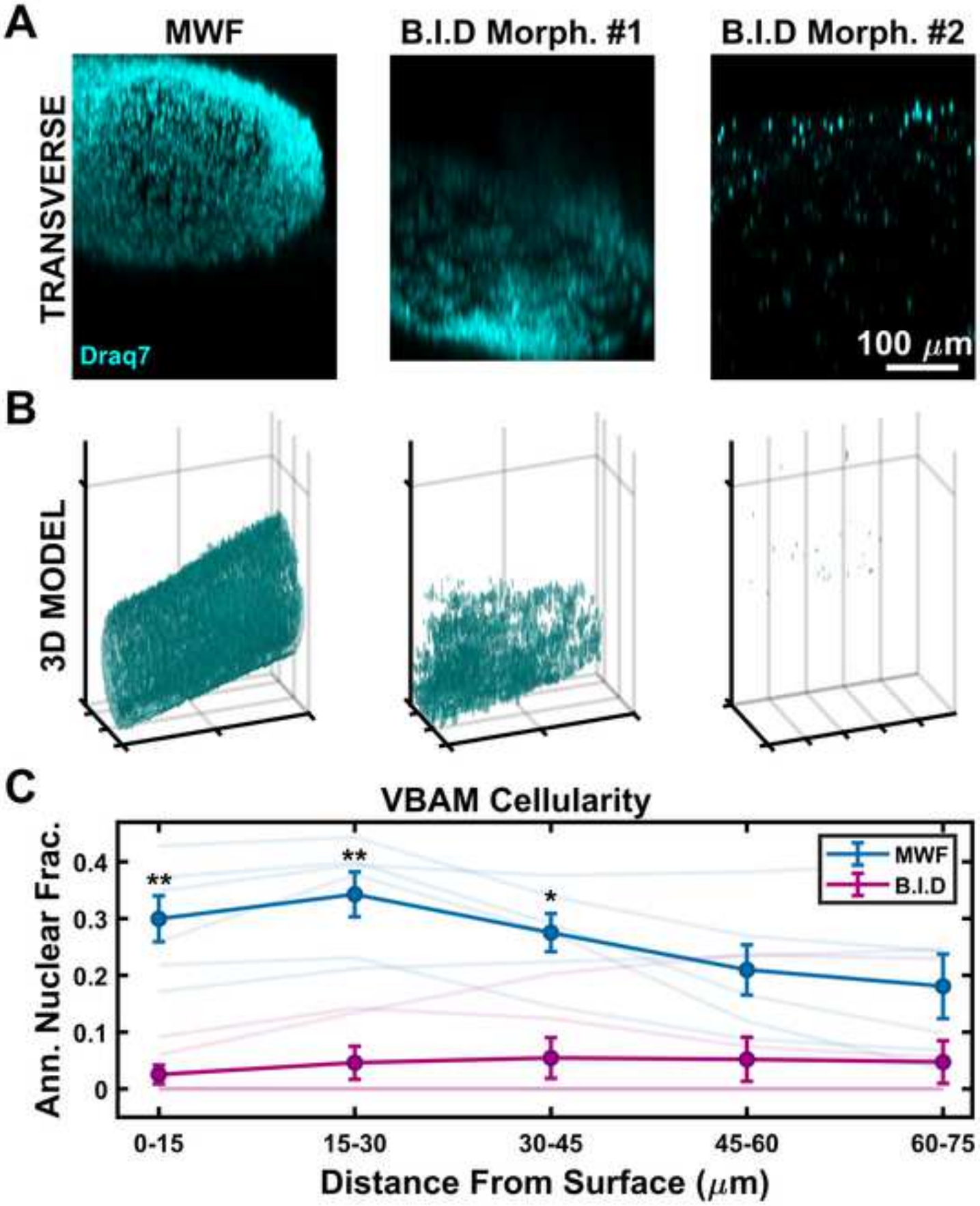
A
MWF
B.I.D Morph. #1
B.I.D Morph. #2
TRANSVERSE
Draq7
100 μm
B
3D MODEL
C
VBAM Cellularity
Ann. Nuclear Frac.
0.4
0.3
0.2
0.1
0
**
**
*
MWF
B.I.D
0-15
15-30
30-45
45-60
60-75
Distance From Surface (μm)